



Scuola Superiore di Catania
Classe delle scienze sperimentali



AMOLF
Department of Nanophotonics



The University of Texas at Austin
Electrical and Computer Engineering

Andrea CORDARO

ALL-OPTICAL COMPUTING METASURFACES

**HIGH-INDEX DIELECTRIC METASURFACES PERFORMING
MATHEMATICAL OPERATIONS**

Advisors:	Prof. Dr. Albert Polman Prof. Dr. Andrea Alù
Tutor:	Prof. Dr. Francesco Priolo
Opponent:	Prof. Dr. Giulia Tagliabue

A Claudio

*Sole sul tetto dei palazzi in costruzione
Sole che batte sul campo di pallone
E terra e polvere che tira vento
E poi magari piove
Nino cammina che sembra un uomo
Con le scarpette di gomma dura
Dodici anni e il cuore pieno di paura.
Ma Nino non aver paura di sbagliare un calcio di rigore
Non è mica da questi particolari
Che si giudica un giocatore
Un giocatore lo vedi dal coraggio
Dall'altruismo e dalla fantasia.
E chissà quanti ne hai visti e quanti ne vedrai
Di giocatori tristi che non hanno vinto mai
Ed hanno appeso le scarpe a qualche tipo di muro
E adesso ridono dentro al bar
E sono innamorati da dieci anni
Con una donna che non hanno amato mai
Chissà quanti ne hai veduti
Chissà quanti ne vedrai.
Nino capì fin dal primo momento
L'allenatore sembrava contento
E allora mise il cuore dentro le scarpe
E corse più veloce del vento
Prese un pallone che sembrava stregato
Accanto al piede rimaneva incollato
Entrò nell'area tirò senza guardare
Ed il portiere lo fece passare
Ma Nino non aver paura di tirare un calcio di rigore
Non è mica da questi particolari
Che si giudica un giocatore
Un giocatore lo vedi dal coraggio
Dall'altruismo e dalla fantasia.
Il ragazzo si farà
Anche se ha le spalle strette
Quest'altr'anno giocherà
Con la maglia numero sette*

La leva calcistica della classe '68 - Francesco De Gregori

CONTENTS

Summary	vii
1 Introduction	1
References	5
2 Theory and design	7
2.1 Fourier Optics.	8
2.2 Fano resonance	10
2.3 Design	11
2.4 Optimized transfer functions and numerical tests	16
References	19
3 Experiment	21
3.1 Fabrication	22
3.2 Optical characterization	26
3.2.1 Integrating sphere	26
3.2.2 Duimelij n Fourier microscope	26
References	31
4 Conclusion	33
Acknowledgements	37
A Appendix	39
A.1 Scattering matrix formalism	39
A.2 Coupled Mode Theory	40
A.2.1 Proofs of properties (A.17) - (A.19)	43
References	46
Curriculum Vitæ	47
List of Publications	49

SUMMARY

Image processing and edge detection are at the core of many newly emerging technologies, such as augmented reality, autonomous driving and more generally object recognition. Image processing is typically performed digitally using integrated electronic circuits and algorithms, implying fundamental speed limitations and significant power needs. It can also be performed instantaneously and at low-power by purely analog Fourier optics, but this requires bulky optical components.

The unprecedented control on light propagation that has been recently achieved by optical metasurfaces opens entirely new opportunities for analog optical computing. In fact, “computing metasurfaces” would benefit from the speed and low power consumption of optics while at the same time being a chip-scale technology compatible with hybrid optical and electronic data processing on a single chip.

Here, we demonstrate for the first time that judiciously engineered silicon metasurfaces can perform mathematical operations and optical image edge detection in a fully analog way. The key to our work is that Fano-resonances in a compact geometry of silicon nanobeam arrays unlock a diversity of operations in the Fourier domain acting on amplitude and phase. We present metasurface designs that perform either 1st- or 2nd-order spatial differentiation. We experimentally demonstrate the 2nd-derivative operation on two-tone and graytone input images, directly showing the potential of all-optical edge detection. A unique advantage of this silicon metasurface geometry is that it operates at a large numerical aperture of 0.35, more than 25 times higher than previously explored schemes, meaning it can be readily integrated in high-performance imaging systems. In addition, it also offers largely enhanced efficiency, ensuring close-to-ideal transmission efficiency for differentiation using passive devices.

1

INTRODUCTION

D' jornu nan ni vogghiu e 'a sira spardu l'ogghiu

Old Sicilian saying

THE amount of data that is being globally created, processed and stored is increasing at a remarkable pace. Furthermore, the advent of new technologies, such as augmented reality (AR), autonomous driving, and many other emerging techniques, requires on-the-fly processing of large data files, such as images, at an increasing rate. Image processing is usually performed digitally but the speed and power consumption limits of standard microelectronic components have become a true bottleneck. Analog optical processing provides a promising route that may overcome these limitations.

While a lot of data is nowadays stored, guided and routed in the optical domain, computing is still performed digitally. The idea of computing optically can be traced back to the early 1960s prompted by pioneering work that ingeniously exploited concepts of Fourier optics [1–4]. Among others, all-optical pattern recognition and optical processing of synthetic-aperture radar (SAR) data were the most successful. The freedom of choice about the linear transformation allowed by a generic spatial filter prompted the idea of designing responses in k -space specific to a certain type of input. This is the concept at the base of matched spatial filters and in turn at the core of optical pattern recognition [5–8]. As shown in Figure 1.1a, an optical processor is able to discriminate the character contained in the input image and signals the answers with a bright spot under the letter “P”. More elaborate approaches even achieved real-time face recognition [9].

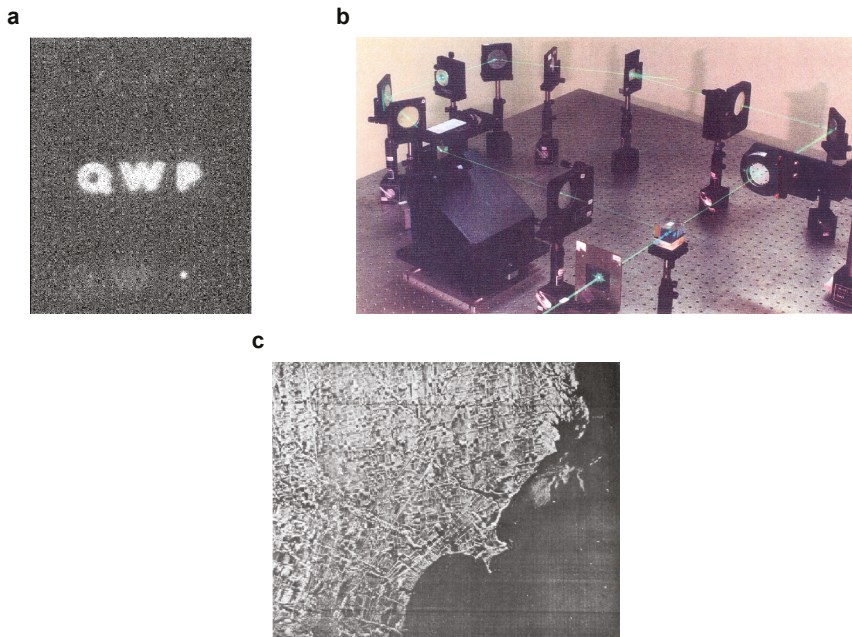


Figure 1.1: **a** A set of matched spatial filters can recognize an input character. The bright spot signals the outcome of the recognition scheme. [10] **b** Photograph of a pattern-recognition system [4] **c** Synthetic-aperture radar image of Monroe, MI (USA) [2]

Fourier optics based optical processors were also successfully used to apply linear transformation on data-sets that are not human readable. Specifically, in the mid 1960s Cutrona

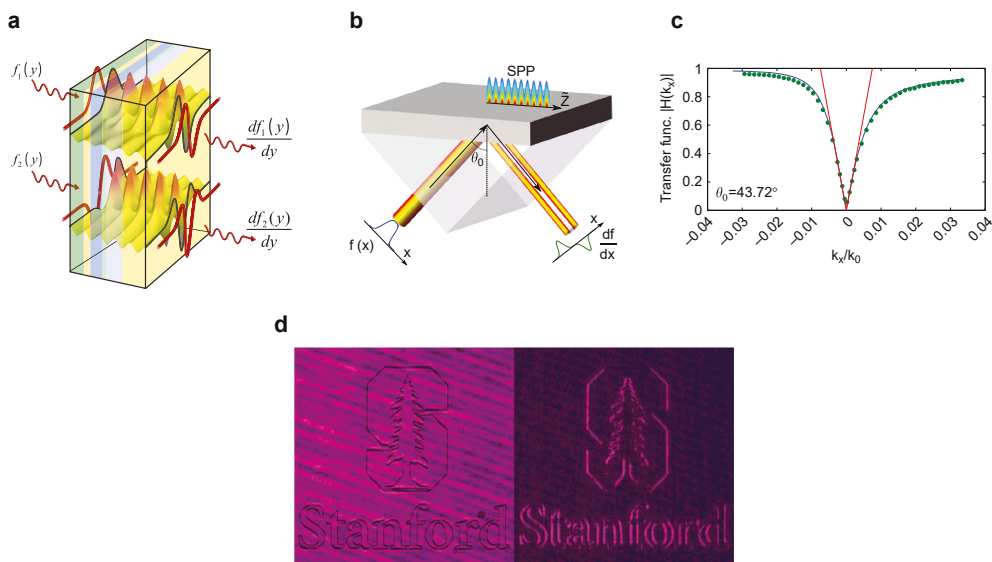


Figure 1.2: **a** Conceptual sketch of a GRIN-based metamaterial performing 1st- or 2nd-order derivative. **b** Plasmonic spatial differentiator exploiting SPP. **c** Spatial transfer function spectra of the sample sketched in b, experimental measurement (dotted lines) and numerical fitting (solid lines). **d** Input image modulated in phase and output image demonstrating edge detection. Re-adapted from [11, 14].

et al.[2] found a way to convert the microwave reflectivity signals acquired by special side-looking airplane radars (SARs) into high-resolution pictures (see Figure 1.1c) These elegant all-optical solutions, however, require bulky optical components that are not integrable into nanophotonic or microelectronic systems; hence, as the transistor size scaled down dramatically and digital computational power skyrocketed, these approaches became quickly obsolete.

The unprecedented control of light propagation over a sub-wavelength thickness that has been recently enabled by optical metasurfaces opens entirely new opportunities for analog optical computing [11–16]. In fact, “computing metasurfaces” may benefit from the speed and low power consumption of optics while being amenable to on-chip integration, thus enabling hybrid optical and electronic data processing on a single chip. In this context the work of Silva et al.[11] is groundbreaking as it introduced the idea of using suitably designed metamaterials to perform arbitrary mathematical operations. As conceptually illustrated in Figure 1.2a, a series of optimized graded-index (GRIN) dielectric slabs can transform a given input wave signal $f(y)$ into its 1st- or 2nd-order derivative. Although the high conceptual impact, this approach remained experimentally unpractical given the complexity of the design.

More recently, a simpler approach based on plasmonic resonances [14] demonstrated experimentally all-optical edge detection. This work exploits the possibility of coupling to Surface Plasmon Polaritons (SPP) at the interface between air and metal by means of a prism (Kretschmann configuration)[17]. Indeed, for a given metal thickness, light is efficiently coupled only at a specific angle due to momentum matching while the metal

surface is completely reflective when this condition is not met. This, in turn, results into a sharp dip in the transfer function of the system which can be used efficiently as an high pass filter (see Figure 1.2b-d): the edges of input image (Stanford tree logo) modulated in phase are enhanced in the output image as a result of the spatial filtering. The drawbacks of this configuration are the limited NA and the use of bulky elements: while the former ($NA \sim 0.01$) implies low spatial resolution and does not allow readily integration in imaging system (which usually have larger NA), the latter further limits any possible on-chip implementation.

In recent theoretical work [15, 16] the same group designed photonic crystal slabs spatial filters reducing greatly the device footprint. However, also in this cases the NA is ~ 0.01 .

OUTLINE OF THE THESIS

We introduce dielectric metasurfaces that perform optical image edge detection in the analog domain using a sub-wavelength geometry that can be readily integrated with detectors. The metasurface is composed of a suitably engineered array of nanobeams designed to perform either 1st- or 2nd-order spatial differentiation. We experimentally demonstrate the 2nd-derivative operation on an input image, showing the potential of all-optical edge detection using a silicon metasurface geometry working at a numerical aperture as large as 0.35.

In Chapter 2 the theoretical foundations of our work are presented. A brief section reviews the concepts of Fourier Optics needed throughout the thesis and the idea of using Fano resonances to design the transfer function is explained. A simple design recipe shows how to tailor the spatial dispersion of the metasurface and finally the optimized transfer functions are tested numerically.

Chapter 3 deals with the experimental efforts related to this work. First, the fabrication process is described step by step both for the metasurface and for the images that are used as diapositives. Next, the fabrication results are commented and the samples' optical characterization is discussed. The optical setups used are described along with the measurements. Finally, the experimental 2nd-order differentiation is compared to its ideal counterpart showing significant agreement.

Lastly, Appendix A contains parts of the lengthy calculations supporting Chapter 2, including the Couple-Mode-Theory derivation needed in the design recipe and a brief recap of the scattering matrix formalism.

REFERENCES

- [1] D. Psaltis and R. A. Athale, *High accuracy computation with linear analog optical systems: a critical study*, *Applied Optics* **25**, 3071 (1986).
- [2] L. J. Cutrona, E. N. Leith, L. J. Porcello, and W. E. Vivian, *On the Application of Coherent Optical Processing Techniques to Synthetic-Aperture Radar*, *Proceedings of the IEEE* **54**, 1026 (1966).
- [3] R. Athale and D. Psaltis, *Optical Computing: Past and Future*, *Optics and Photonics News* **27**, 32 (2016).
- [4] Y. S. Abu-Mostafa and D. Psaltis, *Optical Neural Computers*, *Scientific American* **256**, 88 (1987).
- [5] J. D. Armitage and A. W. Lohmann, *Character recognition by incoherent spatial filtering*, *Applied Optics* **4**, 461 (1965).
- [6] H. J. Caulfield and W. T. Maloney, *Improved discrimination in optical character recognition*, *Applied Optics* **8**, 2354 (1969).
- [7] D. L. Flannery and J. L. Horner, *Fourier optical signal processors*, *Proceedings of the IEEE* **77**, 1511 (1989).
- [8] A. Lugt, *Coherent optical processing*, *Proceedings of the IEEE* **62**, 1300 (1974).
- [9] H. Y. S. Li, Y. Qiao, and D. Psaltis, *Optical Network For Real-time Face Recognition*, *Applied Optics* **32**, 5026 (1993).
- [10] J. W. Goodman, *Introduction to Fourier Optics*, 4th ed. (W. H. Freeman, 2017).
- [11] A. Silva, F. Monticone, G. Castaldi, V. Galdi, A. Alu, and N. Engheta, *Performing Mathematical Operations with Metamaterials*, *Science* **343**, 160 (2014).
- [12] H. Kwon, D. Sounas, A. Cordaro, A. Polman, and A. Alù, *Nonlocal Metasurfaces for Optical Signal Processing*, *Physical Review Letters* **121**, 173004 (2018).
- [13] A. Roberts, D. E. Gómez, and T. J. Davis, *Optical image processing with metasurface dark modes*, *Journal of the Optical Society of America A* **35**, 1575 (2018).
- [14] T. Zhu, Y. Zhou, Y. Lou, H. Ye, M. Qiu, Z. Ruan, and S. Fan, *Plasmonic computing of spatial differentiation*, *Nature Communications* **8**, 15391 (2017).
- [15] C. Guo, M. Xiao, M. Minkov, Y. Shi, and S. Fan, *Isotropic wavevector domain image filters by a photonic crystal slab device*, *Journal of the Optical Society of America A* **35**, 1685 (2018).
- [16] C. Guo, M. Xiao, M. Minkov, Y. Shi, and S. Fan, *Photonic crystal slab Laplace operator for image differentiation*, *Optica* **5**, 251 (2018).
- [17] S. A. Maier, *Plasmonics: Fundamentals and Applications*, 1st ed. (Springer US, New York, NY, 2007).

2

THEORY AND DESIGN

This chapter lays the theoretical foundations of our work. Specifically, the first section will briefly review known notions of Fourier Optics defining concepts that are useful throughout the thesis. Next, the idea of using a Fano resonant metasurface as a spatial filter is introduced. Section 2.3 describes how to tailor the spatial dispersion of the metasurface by manipulating its leaky modes dispersion and the related Fano resonance asymmetry and linewidth. Finally, in Section 2.4 the optimized transfer functions are used to numerically test how well the ideal 1st– and 2nd–order differentiation are approximated by our realistic metasurface designs.

Parts of the lengthy calculations supporting this Chapter are in Appendix A.

The first part of Section 2.1 dealing with Fourier optics follows the notation and the description of Ref.[1].

2.1. FOURIER OPTICS

AN arbitrary two-dimensional input wave signal (i.e. an image) can be represented in general by a complex function $f(x, y)$. If the latter function is absolutely integrable (i.e. $f \in L^1(\mathbb{R}^2)$) it can be thought as the superposition of spatial harmonic functions of the form

$$F(v_x, v_y) \exp[i2\pi(v_x x + v_y y)] \quad (2.1)$$

where $F(v_x, v_y)$ is a complex amplitude and v_x, v_y are called *spatial frequencies* and define the harmonic functions' periodicities $\Lambda_x = 1/v_x$ and $\Lambda_y = 1/v_y$ along the x and y directions. This concept is intuitively shown in Figure 2.1 and can be rigorously formalized as

$$f(x, y) = \iint_{-\infty}^{\infty} F(v_x, v_y) \exp[i2\pi(v_x x + v_y y)] dv_x dv_y. \quad (2.2)$$

where $F(v_x, v_y)$ is the Fourier transform of $f(x, y)$. Next, it is important to show that these harmonic functions can be mapped one-to-one to simple plane waves (see Figure 2.2a). In fact, any arbitrary harmonic function can be seen as a slice of the monochromatic plane wave $U(x, y, z) = A \exp[i(k_x x + k_y y + k_z z)]$, with wavevector $\vec{k} = (k_x, k_y, k_z)$, complex amplitude A and wavelength λ , at the plane $z = 0$, provided that $k_x = 2\pi v_x$ and $k_y = 2\pi v_y$. Vice-versa, the knowledge of the spatial frequencies of an harmonic function completely determines the corresponding plane wave as the knowledge of k_x and k_y is sufficient to determine the k_z via the relation $k_x^2 + k_y^2 + k_z^2 = 2\pi/\lambda^2$.

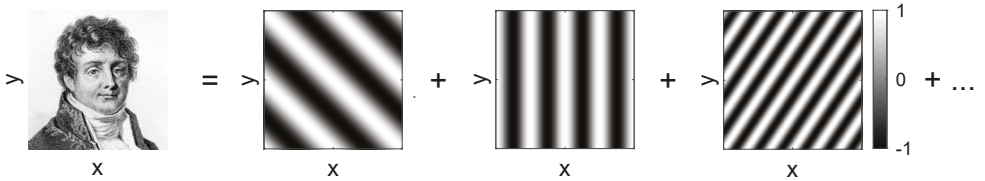


Figure 2.1: An arbitrary image can be expanded into a set of harmonic functions. Here the real part of Eq. (2.1) is plotted for three couples (v_x, v_y) and $F(v_x, v_y) = 1$.

Suppose that a monochromatic plane wave with unit amplitude propagating along the z axis impinges on thin optical element (e.g. a transparency or a diapositive) with a certain complex transmission function $f(x, y)$. All the harmonic functions composing $f(x, y)$ can be seen as a slice of a corresponding plane wave propagating in a certain direction making angles $\theta_x = \arcsin(\lambda v_x)$ and $\theta_y = \arcsin(\lambda v_y)$ with the y - z and x - z planes, respectively. Hence, as the plane wave is passing through the transparency it is also dispersed into its spatial components and transmitted wave $U(x, y, z)$ is a superposition of plane waves

$$U(x, y, z) = \iint_{-\infty}^{\infty} F(v_x, v_y) \exp[i2\pi(v_x x + v_y y)] \exp(ik_z z) dv_x dv_y. \quad (2.3)$$

This bundle of plane waves, schematically illustrated in Figure 2.2b, is the spatial content of the image and contains its information just as $f(x, y)$ does. Manipulating the plane

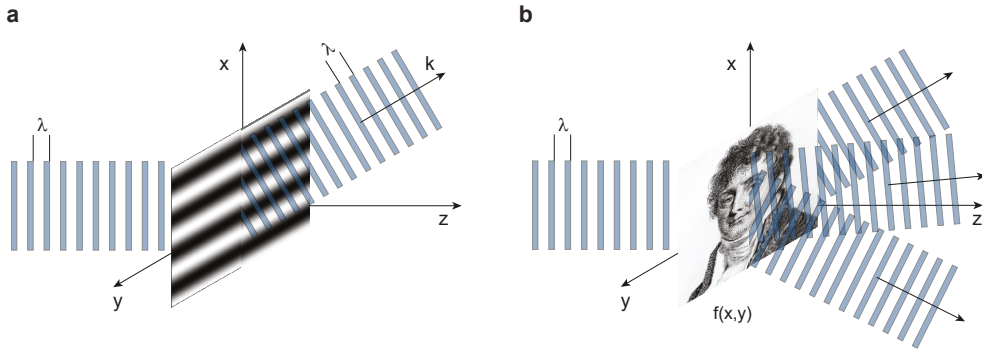


Figure 2.2: **a** A thin optical element that has a complex transmission equal to the harmonic function $\exp[i2\pi v_x x]$ bends light at an angle $\theta_x = \arcsin(\lambda v_x)$. This is the working principle of a phase grating. **b** the same concept can be extended to an arbitrary complex transmission $f(x, y)$ composed of many harmonic functions.

waves composing it is equivalent to performing a certain operation on $f(x, y)$ itself.

The advantage of such theoretical framework becomes clear when dealing with arbitrary traveling waves that are interacting with optical systems. Indeed, if the system response is known for every plane wave composing the arbitrary input signal then output can be readily calculated. In particular, if the two dimensional optical system relating an input function $f_1(x, y)$ to the output function $f_2(x, y)$ is *linear* and *shift-invariant* (or isoplanatic)¹ then

$$F_2(v_x, v_y) = H(v_x, v_y)F_1(v_x, v_y) \quad (2.4)$$

where $F_1(v_x, v_y)$ and $F_2(v_x, v_y)$ are the Fourier transforms of f_1 and f_2 and $H(v_x, v_y)$ is a function describing the response of the optical system to plane waves called *transfer function*. Intuitively, by modulating its spatial content, $H(v_x, v_y)$ transforms $f_1(x, y)$ into $f_2(x, y)$.

Among the vast realm of operations, n^{th} -order spatial differentiation is of great appeal in the field of augmented reality and object recognition. In fact, performing the derivative of an image reveals its edges and, in turn, edge detection is a fundamental tool for object recognition. Thus, it is important to assess what transfer function corresponds to the latter operation. Moving to the 1D case, if $f(x)$ is an arbitrary wave input signal, then its n^{th} -order derivative $\frac{d^n f(x)}{dx^n}$ equals $(ik_x)^n F(k_x)$ in the spatial domain, where $F(k_x)$ is the Fourier transform of $f(x)$. Thus, the transfer function corresponding to the n^{th} -order derivative is $H(k_x) = (ik_x)^n$.

Proof. $\frac{d^n f(x)}{dx^n} \rightarrow (ik_x)^n F(k_x)$

Suppose $f(x)$ is an arbitrary function $\in L^1(\mathbb{R})$ and let us introduce the notation $\mathcal{F}[f(x)]$

¹A system is said linear if the response to the sum of any linear combination of inputs is the linear combination of the responses to each input. A system is said isoplanatic if a shift to the input function in space corresponds to the same shift in output.

for the Fourier transform of $f(x)$

$$\mathcal{F}[f(x)] = \int_{-\infty}^{\infty} f(x) e^{-ik_x x} dx \quad (2.5)$$

then the transform of the first derivative $f'(x)$ of the function reads

$$\mathcal{F}[f'(x)] = \int_{-\infty}^{\infty} f'(x) e^{-ik_x x} dx \quad (2.6)$$

This integral can be solved by parts

$$\int_{-\infty}^{\infty} f'(x) e^{-ik_x x} dx = f(x) e^{-ik_x x} \Big|_{-\infty}^{+\infty} + ik_x \int_{-\infty}^{\infty} f(x) e^{-ik_x x} dx \quad (2.7)$$

the first term goes to zero since $f \in L^1(\mathbb{R})$ while the second term is just $\mathcal{F}[f(x)]$. Hence

$$\mathcal{F}[f'(x)] = ik_x \mathcal{F}[f(x)] \quad (2.8)$$

and the transfer function corresponding to 1st-order derivative is $H_1 = ik_x$. Repeating this procedure n times demonstrates the property $\frac{d^n f(x)}{dx^n} \rightarrow (ik_x)^n F(k_x)$. \square

As a consequence, 2nd-order differentiation can be achieved by a metasurface that has a parabolic transfer function which modulates the spatial frequencies composing the input signal[1, 2]. If the metasurface can be treated as a simple two-ports optical system (i.e. no extra diffraction channels are opened other than the 0th-order) then the system's transfer function coincides with scattering matrix element representing transmission S_{21} (see Appendix A for a brief introduction to the scattering matrix formalism). Hence, from now on, $S_{21}(k_x)$ will be also referred to with the term transfer function. As explained within next paragraph, we introduce the idea of using a Fano-resonant metasurface to design a specific angular transmission response and therefore $S_{21}(k_x)$.

2.2. FANO RESONANCE

In this work, we design and realize optical metasurfaces composed of dielectric nanobeams that are illuminated by light polarized along the beams' direction. We tailor the spatial dispersion of the metasurfaces by controlling the leaky modes guided along the surface[3–6]. Indeed, when the frequency and in-plane wave vector of incident light match one of these quasi-guided modes, an asymmetric Fano line-shape appears in the transmission spectrum [7–9], due to interference with the broad Fabry-Pérot resonance determined by the thickness and fill fraction of the structure. Figure 2.3a shows simulated transmission S_{21} spectra of an array of dielectric nanobeams (width $w = 182$ nm, height $h = 123$ nm, pitch $p = 250$ nm and refractive index $n = 4$ typical for Si) for incident angles ranging from 0 to 0.3 radians (17°). Due to the Fano interference, the transmission swings from 0 to unity within a narrow bandwidth. The sharp response in frequency corresponds to strong non-locality: the spectrum is largely dependent on the incident angle and the transmission minimum shifts from $\lambda = 633$ nm to $\lambda = 618$ nm over the simulated angular range. The strong amplitude variation in transmission, and the sensitivity to the incoming k-vector, are often undesirable features of resonant metasurfaces, yet here these

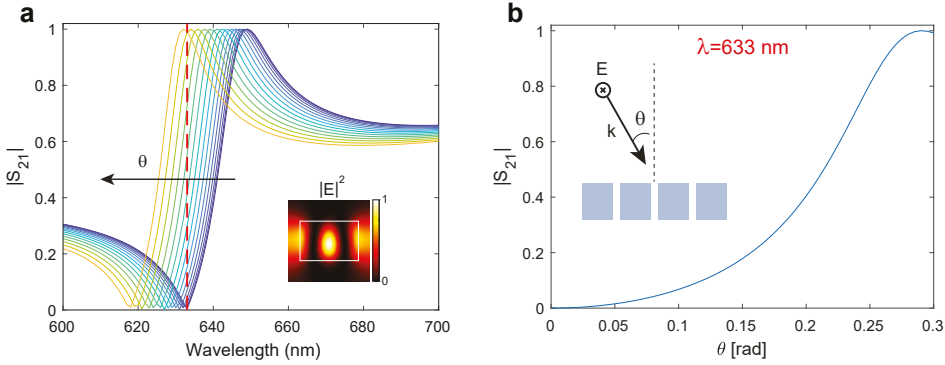


Figure 2.3: **a** Fano-resonant metasurface transmission spectra. Simulated transmission spectra of a metasurface consisting of an array of dielectric nanobeams (width $w = 182$ nm, height $h = 123$ nm, pitch $p = 250$ nm and refractive index $n = 4$) as the incident angle is changed from 0 (blue line) to 0.3 rad (yellow line) in 15 steps. The red dashed line indicates the wavelength of operation ($\lambda = 633$ nm). **b** Cross-cut through **a** showing the transmission at $\lambda = 633$ nm as the incidence angle θ is changed. Insets: electric field amplitude profile within a unit cell at the resonant wavelength; schematic of the proposed structure showing incoming light polarization.

features enable the use of the metasurface as a Fourier spatial filter, and tailor with large flexibility its angular transmission response and thus transfer function. In fact, by tuning the dispersion of the quasi-guided mode resonance, as well as the Fano line-shape asymmetry and linewidth, it is possible to design an optimized transfer function for a specific excitation wavelength (see Figure 2.3b), as described in the next paragraph.

2.3. DESIGN

The main idea behind our designs of metasurfaces for image processing is that their transfer function can be tuned by introducing a Fano resonance in transmission, and manipulating its dispersion asymmetry and linewidth. In order to prove this property, we use the general formula for a Fano lineshape [8, 10]

$$|S_{21}| = \frac{(\epsilon + q)^2}{\epsilon^2 + 1} m, \quad (2.9)$$

where S_{21} is the scattering matrix element representing transmission for a generic two-port optical system, $m = 1/(1+q^2)$ is a normalization factor, and $\epsilon(k_x) = 2(\omega - \omega_0(k_x))/\Gamma$ is a dimensionless parameter that traces the detuning of the operation frequency ω relative to the resonance at $\omega_0(k_x)$ (dispersing with wavevector k_x), normalized to the linewidth Γ of the resonance. One way to achieve a dispersive resonance frequency is by using one of the leaky-wave resonances of the metasurface. In this case, incident waves are coupled to surface waves propagating along the metasurface through the additional momentum added to them by the metasurface and $\omega_0(k_x)$ generally follows the dispersion of these surface waves. The variable q is a phenomenological lineshape parameter which reflects the contribution of the discrete state in a Fano resonance relative to that of the continuum. Without specifying the nature of the resonance yet we show how it is possible to

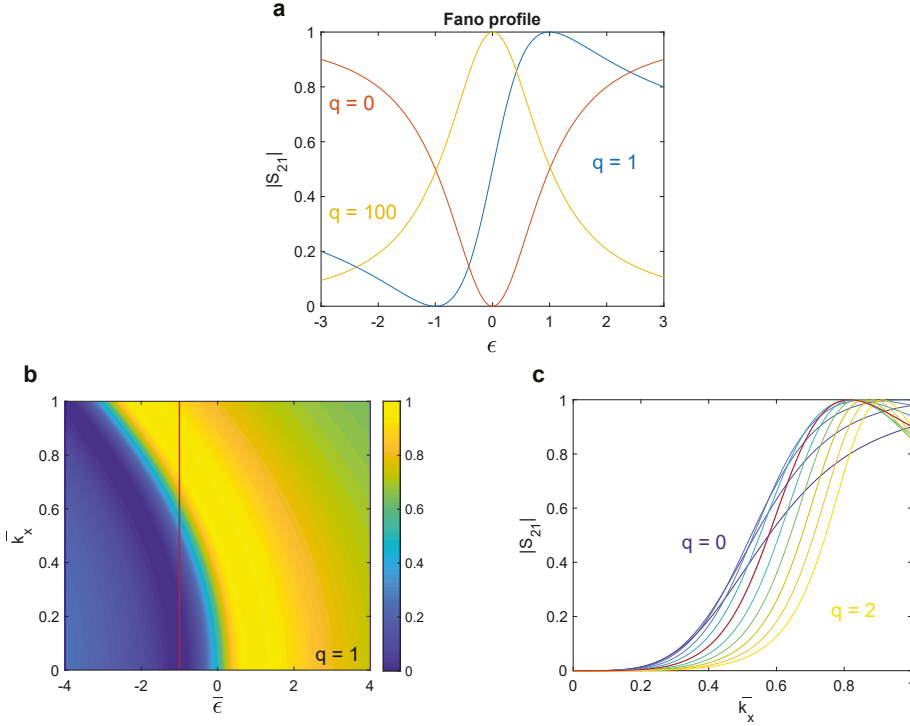


Figure 2.4: **a** Plot of $|S_{21}|$ (from Eq.(2.9)) for $q = 0$ (orange solid line), $q = 1$ (blue solid line), $q = 100$ (yellow solid line). **b** Plot of $|S_{21}|$ (from Eq.(2.9)) as function of $\bar{\epsilon}$ and \bar{k}_x for a parabolic dependence of ω_0 on k_x and fixed values for the shape parameter $q = 1$ and for the linewidth $\Gamma = 1$. **c** Plot of $|S_{21}|$ (from Eq.(2.9)) as a function of \bar{k}_x as q is changed from 0 (blue line) to 2 (yellow line) in steps of 0.2. The red solid line corresponds to the indicated cross-cut through b.

design the transfer function $|S_{21}(k_x)|$ by tuning the parameters in Eq.(2.9). Starting with q , Figure 2.4a shows how it controls the asymmetry of the Fano lineshape: for $q = 0$ the transmission has a symmetrical dip at the $\bar{\epsilon}$ corresponding to the system resonance; for increasing values of q the lineshape evolves from a completely asymmetric one to a standard Lorentzian peak (for $q \rightarrow \infty$, data not shown). In the most general case, $\omega_0(k_x)$ can be expressed as $\omega_0(k_x) = \omega_0(0) + \sum_n \alpha_n \left(\frac{ck_x}{\omega_0(0)}\right)^n$ by applying the Taylor expansion at $k_x = 0$. Note that k_x is normalized versus the free-space wavenumber at $\omega_0(0)$ so that all α_n are expressed in the same frequency units. In reciprocal structures $\omega_0(-k_x) = \omega_0(k_x)$, indicating that all the odd-order terms are zero ($\alpha_1 = \alpha_3 = \dots = 0$). Then, the dominant term in the expansion is the one with $n = 2$, and in Figure 2.4b we plot the transmission as a function of the normalized frequency $\bar{\epsilon} = 2(\omega - \omega_0(0))/\Gamma$ and normalized wavenumber $\bar{k}_x = ck_x/\omega_0(0)$ for fixed values of q and Γ and assuming only the second-order dominant term in the Taylor expansion of $\omega_0(k_x)$ with $\alpha_2 = -3/2$.

Taking a cross cut of the data at the $\bar{\epsilon}$ of the minimum for $k_x = 0$ it is possible to study the behavior of $|S_{21}(k_x)|$ as a function of q . As shown in Figure 2.4c, tuning the asymmetry of the Fano lineshape strongly affects the concavity and shape of the transfer function

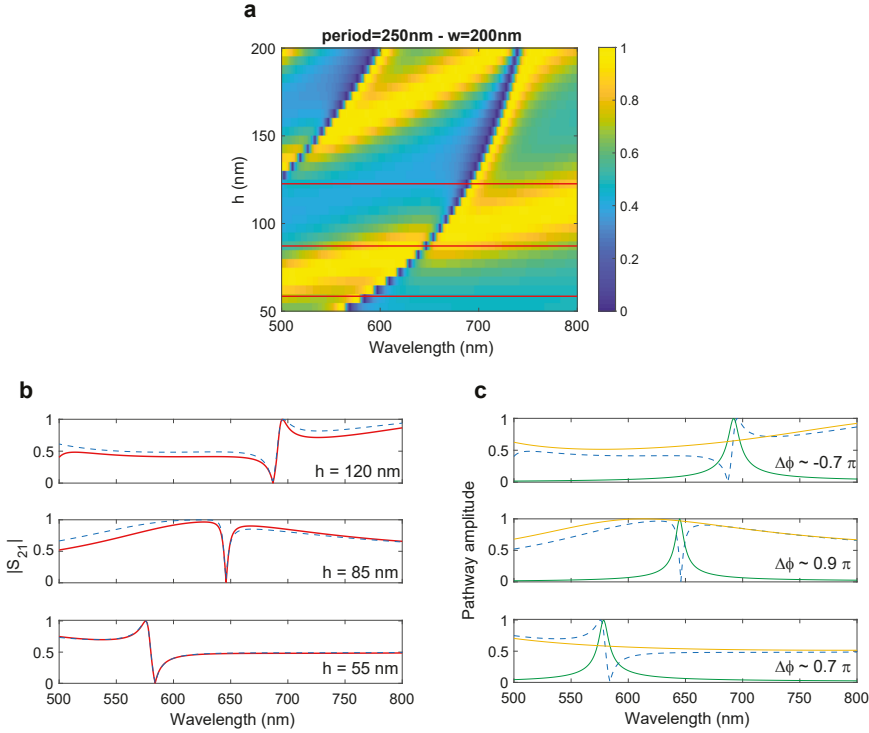


Figure 2.5: **a** Simulated transmission spectra of an array of nanobeams ($n = 4$, $w = 200\text{ nm}$, $p = 250\text{ nm}$) as the height h is swept from 50 nm to 200 nm . The electric field \vec{E} is polarized along the nanobeams. **b** Cross-cuts through **a** for $h = 55\text{ nm}$, $h = 85\text{ nm}$ and $h = 120\text{ nm}$ (red solid lines) and fitted spectra according to coupled-mode theory (blue dashed lines). **c** Amplitude of the direct (yellow) and resonant (green) pathways composing the fits (blue dashed lines).

$|S_{21}(k_x)|$. In particular for $q = 1$ a close-to-parabolic shape can be obtained, similar to what is desired for the optimized 2nd-order differentiation. It is important that, in actual realizations, also q and Γ might disperse with k_x but for the sake of simplicity this is not taken into account here.

Next, we discuss how the structural parameters of the metasurface are connected to the variables just described. While there is no trivial way to design $\omega_0(k_x)$, it is straightforward to tune q . Figure 2.5a shows the simulated transmission spectra of an array of nanobeams (refractive index $n = 4$) with fixed width ($w = 200\text{ nm}$) and periodicity ($p = 250\text{ nm}$) as the height h is swept from 50 nm to 200 nm . It is easy to notice how the asymmetry of the Fano line shape changes as h is increased (see Figure 2.5b). The Fano lineshapes for this type of metasurfaces are induced by the interference between sharp quasi-guided modes that can be launched in-plane along the structure and a broader Fabry-Pérot (FP) background determined by the fill fraction F and the height h of the structure; these two different light pathways correspond to spectral features that are easily distinguishable in Figure 2.5a. Changing the height of the structure shifts the frequency response of both pathways and thereby controls the amplitude and phase at

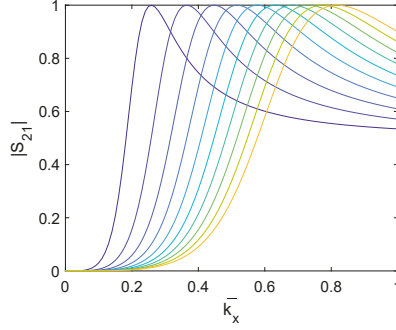


Figure 2.6: Plot of $|S_{21}|$ (from Eq.(2.9)) as function of k_x for a parabolic dependence of ω_0 on k_x with $\alpha_2 = -3/2$ and a fixed shape parameter $q = 1$ as Γ is increased from 0.1 (blue line) to 1 (yellow line).

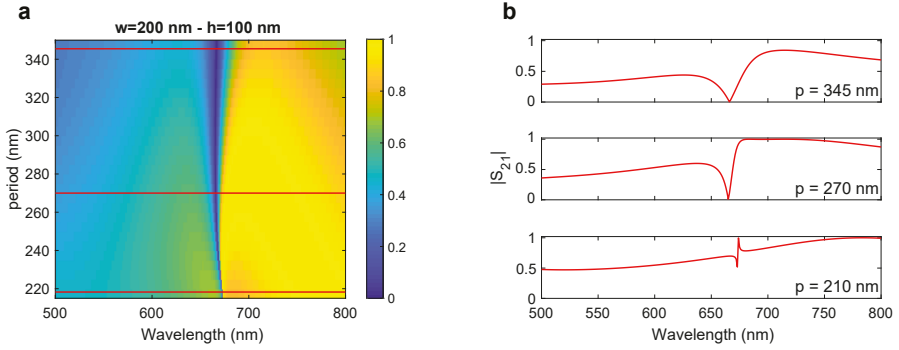


Figure 2.7: **a** Simulated transmission spectra of an array of nanobeams ($n = 4$, $w = 200$ nm, $h = 100$ nm) as the period p is swept from 205 nm to 350 nm. The electric field \vec{E} is polarized along the nanobeams. **b** Cross-cuts through **a** for $p = 210$ nm, $p = 270$ nm and $p = 345$ nm (red solid lines).

which they interfere to generate the asymmetric lineshape. This property is formalized in Coupled-Mode Theory (CMT) [11, 12] that provides an analytical form for the transmission of a system with a guided-mode resonance (see Appendix A)

$$S_{21} = t \pm \frac{-(r \pm t)\gamma}{i(\omega - \omega_0) + \gamma}, \quad (2.10)$$

where ω_0 is the resonance frequency, γ is the radiative leakage rate and r and t are the reflection and transmission Fresnel coefficient for a uniform slab of index $n_{\text{eff}} = [(1-F)n_0^2 + Fn^2]^{1/2}$ (with $n = 4$ and $n_0 = 1$) [13]. Thus, the first term in Eq.(2.10) represents the broad FP background while the second term represents the guided-mode-resonant pathway. Since these two terms are complex valued it is important to study their phase difference $\Delta\phi = \arg(t) - \arg(\pm \frac{-(r \pm t)\gamma}{i(\omega - \omega_0) + \gamma})$ on resonance to understand how the two pathways combine and hence determine the final asymmetry of the Fano resonance. To do this, we fit the simulated transmission of Figure 2.5a for three different heights (see Fig-

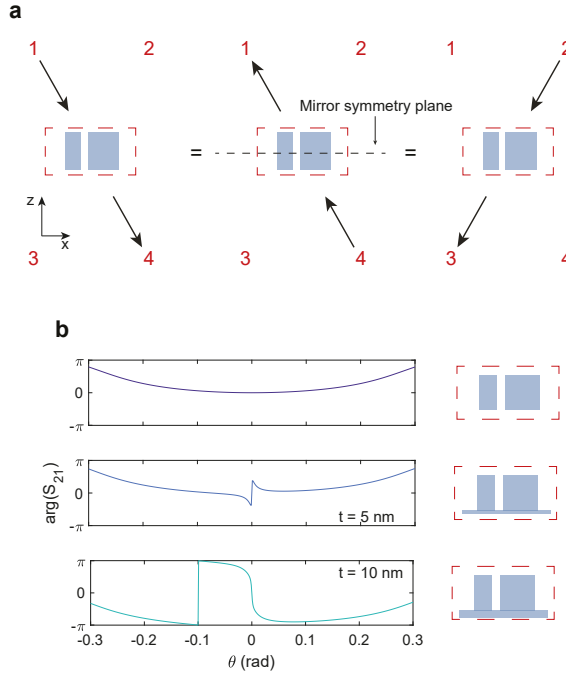


Figure 2.8: **a** The transmission response is still symmetric if only one of the symmetries is broken. **b** Simulated transmission phase of an array of nanobeams ($n = 4$, $w_1 = 40$ nm, $w_2 = 108$ nm, gap between the wires equal to 16 nm, $h = 100$ nm and $p = 250$) as the residual thickness t is increased from 0 to 10 nm. The electric field \vec{E} is polarized along the nanobeams.

ure 2.5b–c) using Eq.(2.10). Figure 2.5c shows the amplitude of the two pathways that are composing the fitted functions (dashed blue lines) as well as their phase difference $\Delta\phi$ at the resonance wavelength (inset) highlighting the importance of this phase lag and its influence on the final resonant lineshape. To conclude, thickness tuning provides a direct handle on the asymmetry parameter in $|S_{21}|$, which in turn gives control over the curvature of the transfer function around $k_x = 0$.

Next, we assess how to control the numerical aperture of operation. This is directly controllable by the linewidth parameter Γ in Eq.(2.9). Figure 2.6 shows $|S_{21}(k_x)|$ for fixed q and a parabolic $\omega_0(k_x)$ as Γ is increased. As the linewidth of the resonance is increased also the metasurface operational wavevector range is expanded. Hence, Γ allows direct tuning of the metasurface numerical aperture (NA). In simulation, it is possible to tune the linewidth by changing the array periodicity while keeping the nanobeam dimensions fixed, as shown in Figure 2.7a–b. However, an upper bound on periodicity is set by the opening of higher order diffraction channels at large pitches. These would complicate the design of the transfer function and drop the efficiency.

In the case of 1st-order differentiation, not only the amplitude of the transfer function $|S_{21}(k_x)|$, but also the phase $\arg(S_{21}(k_x))$ is important. In fact, such operation requires a response that has odd-symmetry around the sample normal $S_{21}(-k_x) = -S_{21}(k_x)$.

In other words, the transmission phase for positive k_x values should be phase-shifted by π compared to that of negative k_x values. In order to achieve this asymmetric phase response, it is necessary to break the unit cell's mirror symmetry both along the propagation (i.e. z -axis) and transverse (i.e. x -axis) directions. Invoking Lorentz reciprocity, it is easy to show that breaking the mirror symmetry only along the x -axis is not sufficient (see Figure 2.8a) to generate a transmission response of odd symmetry. Indeed, the transmission at negative incidence angles (from port 1 to 4) S_{41} has to be equal to the transmission from port 4 to 1, i.e. S_{14} , by reciprocity (see Equation (A.9) of Appendix A). Yet the latter has in turn to be equal to S_{32} if the symmetry along the z -axis is not also broken. Thus, at asymmetry along x yet mirror symmetry in z the transmission remains a symmetric function of k_x . This fact can also be observed in simulation as shown in Figure 2.8b. Adding a residual layer of thickness t below the nanobeams breaks the symmetry along the z -axis, and thereby provides the odd-symmetry system response required for odd-order differentiation. Simulations show that the thickness t provides control over the phase asymmetry (see Figure 2.8b).

2.4. OPTIMIZED TRANSFER FUNCTIONS AND NUMERICAL TESTS

Using the insight gained from the previous paragraph it is possible to design metasurfaces with specific transfer functions optimized for 1st- and 2nd-order spatial differentiation. Figure 2.9a shows the simulated transmission amplitude $|S_{21}|$ and phase $\arg(S_{21})$ as a function of the in-plane wave vector k_x , normalized by the free space wavevector k_0 at the design wavelength $\lambda = 633$ nm for a metasurface composed of dielectric nanobeams (width $w = 182$ nm, height $h = 123$ nm, pitch $p = 250$ nm and refractive index $n = 4$ typical for Si). In this design, optimized to perform 2nd-order differentiation, the angular response is close in amplitude to the ideal parabolic shape. The phase response shows a variation of approximately 0.9π , deviating at high angles from the ideal constant phase response, but still providing a close-to-ideal second derivative response.

Our metasurface design has two key features that distinguish it from earlier designs. First of all, the metasurface operational numerical aperture is large ($\text{NA} \approx 0.35$). This feature enables processing images with high spatial content and hence a resolution close to the diffraction limit. Moreover, it allows for direct implementation into standard imaging systems with similar NA, for instance by placing the metasurface right in front of a charge-coupled device (CCD) detector array, without needs for additional imaging lenses. This is a major advance over previously explored spatial differentiation schemes [14–16] that operate at an NA that is ≈ 25 times smaller than what we demonstrate here. Second, the transmission in our design reaches unity at large wavevectors, enabling close-to-ideal image transformation efficiency, significantly larger than earlier attempts at realizing image processing metasurfaces.

Next, we use the optimized transfer function to numerically test how well the ideal 2nd-order differentiation is approximated by our realistic metasurface design. To this end, some simple input functions (see Figure 2.9b-e) are discretized into 1000 pixels and Fourier transformed. The pixel size Δ_x set such that the Nyquist frequency (i.e. the spatial sampling frequency) $\nu_n = 1/\Delta_x$ is equal to $k_{\max}/2\pi$ where k_{\max} is the maximum k_x -vector that the metasurface can process. This choice ensures that the Nyquist range

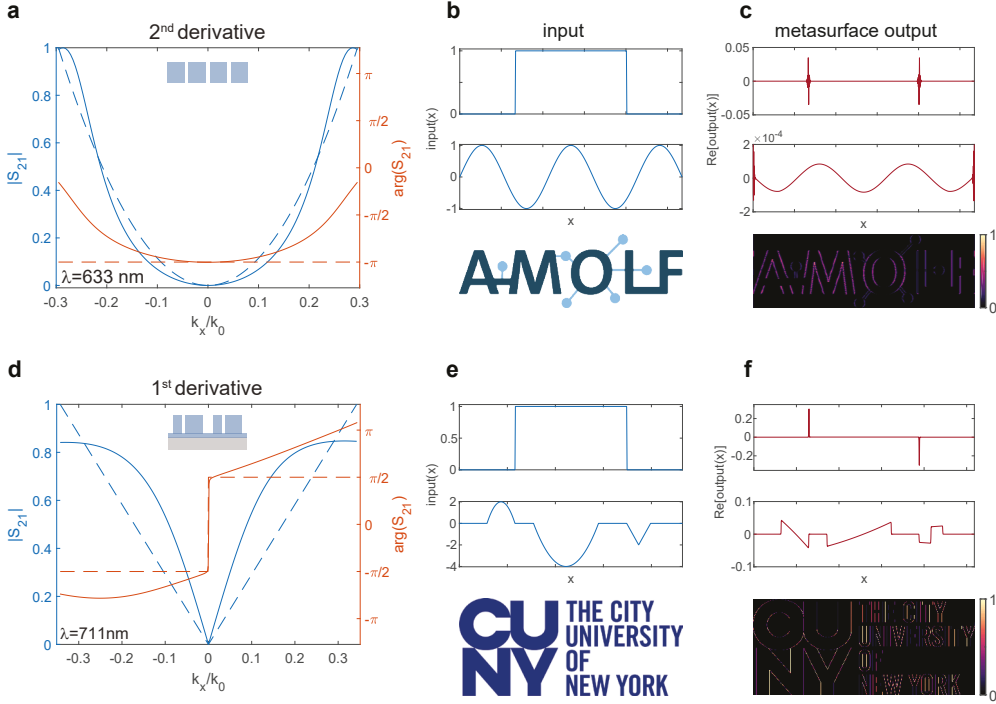


Figure 2.9: Simulated transfer functions of dielectric metasurfaces performing 1st- and 2nd-order spatial differentiation. **a** Transmission amplitude $|S_{21}|$ (solid blue line) and phase $\arg(S_{21}(k_x))$ (solid orange line) for the metasurface optimized for 2nd-derivative operation (sketched in the inset) at $\lambda = 633$ nm. The simulated transfer function is compared to the ideal case (dashed lines). The transmission reference plane is set such that the transmission phase at normal incidence equals $-\pi$. **b** Rectangular and sinusoidal input functions and 2D image that are used to numerically test the metasurface operation. The signal is discretized into 1000 pixels with individual pixel size set such that the Nyquist range matches the operational range in k -space of the metasurface. **c** Metasurface output for the input in **b**. For the 2D image, differentiation is performed line by line along the x -axis. **d-f** Same as **a-c**, but for 1st-derivative operation (metasurface geometry sketched in the inset) compared to the ideal case (dashed lines) at $\lambda = 711$ nm. The transmission reference plane is set such that the transmission phase at normal incidence is 0.

$[-v_n, v_n]$ matches the operational range in k -space of the metasurface and physically means that the test images are projected onto the metasurface under an NA that matches that of the metasurface. Once the input function is Fourier transformed, it is multiplied by the transfer function and finally inverse Fourier transformed (recall Eq. (2.4)).

Figure 2.9c shows the calculated response for rectangular and sinusoidal input functions shown in Figure 2.9b. The metasurface output clearly shows the edges of the rectangular input profile and flips the sinusoidal input function as expected. It is also possible to process arbitrary 2D images by performing the 2nd derivative line by line. The edges of one of our institutions' logos are clearly visible in Figure 2.9c. Notice that differentiation is performed only along the x -axis for this 1D geometry, hence the edges along the same direction are not detected. To illustrate the flexibility of the metasurface image processing concept, Figure 2.9d shows the optimized transmission for a metasurface performing 1st-order differentiation, which corresponds to the transfer function $S_{21}(k_x) = ik_x$ in the Fourier domain. In order to achieve such an operation with odd symmetry in space, we designed an asymmetric metasurface composed of an array of Si nanobeams with a unit cell ($p = 300$ nm) consisting of nanobeams with two different widths ($w_1 = 48$ nm, $w_2 = 96$ nm, $h = 165$ nm and gap between the nanobeams 53 nm), placed on a thin silicon layer (thickness $t = 35$ nm) on a semi-infinite Al_2O_3 substrate. As explained earlier, by Lorentz reciprocity, it is easy to prove that the unit cell has to be asymmetric both along the direction of propagation and transversally. Furthermore, the asymmetry in the phase response of the transfer function can be tuned with t , enabling the required π phase jump at $k_x = 0$. In this case, the experimental optical constants (including losses) for the two materials have been used in the simulations [17, 18]. The simulated transfer function amplitude shows a linear behavior over a wavevector range up to $k_x/k_0 = 0.1$ (6°), above which it gradually bends away from the ideal case. For large angles, the transmission saturates below unity due to intrinsic absorption in Si. Figure 2.9e-f shows the calculated metasurface output for rectangular, parabolic and triangular input functions. The input slope changes and a nearly linear derivative for the parabola are clearly resolved. Furthermore, processing the logo results in clear detection of the edges in the x -direction consistently with 1st-derivative operation.

To conclude, the results shown in this Chapter demonstrate the possibility of designing metasurfaces featuring transfer functions that allow even- and odd-symmetric operations. These optimized designs are composed of nanostructures that can be realistically fabricated and experimentally tested, as shown within next Chapter.

REFERENCES

- [1] B. E. A. Saleh and M. C. Teich, *Fundamentals of Photonics*, Wiley Series in Pure and Applied Optics (Wiley, 2007).
- [2] J. W. Goodman, *Introduction to Fourier Optics*, 4th ed. (W. H. Freeman, 2017).
- [3] S. Fan and J. D. Joannopoulos, *Analysis of guided resonances in photonic crystal slabs*, *Physical Review B* **65**, 235112 (2002).
- [4] G. Pitruzzello and T. F. Krauss, *Photonic crystal resonances for sensing and imaging*, *Journal of Optics (United Kingdom)* **20** (2018), 10.1088/2040-8986/aac75b.
- [5] S. S. Wang and R. Magnusson, *Theory and applications of guided-mode resonance filters*, *Applied Optics* **32**, 2606 (1993).
- [6] S. S. Wang, M. G. Moharam, R. Magnusson, and J. S. Bagby, *Guided-mode resonances in planar dielectric-layer diffraction gratings*, *Journal of the Optical Society of America A* **7**, 1470 (1990).
- [7] B. Luk'yanchuk, N. I. Zheludev, S. A. Maier, N. J. Halas, P. Nordlander, H. Giessen, and C. T. Chong, *The Fano resonance in plasmonic nanostructures and metamaterials*, *Nature Materials* **9**, 707 (2010).
- [8] A. E. Miroshnichenko, S. Flach, and Y. S. Kivshar, *Fano resonances in nanoscale structures*, *Reviews of Modern Physics* **82**, 2257 (2010).
- [9] L. Andreani and M. Agio, *Photonic bands and gap maps in a photonic crystal slab*, *IEEE Journal of Quantum Electronics* **38**, 891 (2002).
- [10] U. Fano, *Sullo spettro di assorbimento dei gas nobili presso il limite dello spettro d'arco*, *Il Nuovo Cimento* **12**, 154 (1935).
- [11] S. Fan, W. Suh, and J. D. Joannopoulos, *Temporal coupled-mode theory for the fano resonance in optical resonators*, *Journal of the Optical Society of America. A* **20**, 569 (2003).
- [12] H. A. Haus, *Waves and fields in optoelectronics* (Prentice-Hall, Englewood Cliffs, N.J, 1984) p. 402.
- [13] D. L. Brundrett, E. N. Glytsis, and T. K. Gaylord, *Homogeneous layer models for high-spatial-frequency dielectric surface-relief gratings: conical diffraction and antireflection designs*, *Applied Optics* **33**, 2695 (1994).
- [14] C. Guo, M. Xiao, M. Minkov, Y. Shi, and S. Fan, *Isotropic wavevector domain image filters by a photonic crystal slab device*, *Journal of the Optical Society of America A* **35**, 1685 (2018).
- [15] C. Guo, M. Xiao, M. Minkov, Y. Shi, and S. Fan, *Photonic crystal slab Laplace operator for image differentiation*, *Optica* **5**, 251 (2018).

- [16] T. Zhu, Y. Zhou, Y. Lou, H. Ye, M. Qiu, Z. Ruan, and S. Fan, *Plasmonic computing of spatial differentiation*, *Nature Communications* **8**, 15391 (2017).
- [17] M. A. Green, *Self-consistent optical parameters of intrinsic silicon at 300K including temperature coefficients*, *Solar Energy Materials and Solar Cells* **92**, 1305 (2008).
- [18] I. H. Malitson and M. J. Dodge, *Refractive Index and Birefringence of Synthetic Sapphire*, in *Program of the 1972 Annual Meeting of the Optical Society of America*, Vol. 62 (1972) p. 1336.

3

EXPERIMENT

Within this chapter, the theory so far developed is experimentally tested and all-optical 2nd-order differentiation is demonstrated.

In Section 3.1 the fabrication process is described step by step both for the metasurface and for the images used as diapositives. Next, the fabrication results are commented and the samples' optical characterization is discussed. In Section 3.2 the optical setups used are described along with the measurements. Finally, the experimental 2nd-order differentiation is compared to its ideal counterpart showing significant agreement.

3.1. FABRICATION

IN order to demonstrate experimentally the concept of performing all-optically mathematical operations via metasurfaces, two different samples ought to be fabricated: the metasurface itself but also the image that is projected onto it. Both sample fabrication procedures involve electron beam lithography (EBL). This technique consists in scanning a focused electron beam on a surface coated with a layer of e-beam resist, a particular material that undergoes a change in solubility once exposed. Next, immersing the sample in a solvent will dissolve the exposed areas thus creating a mask for a successive etching that will eventually define the structure.

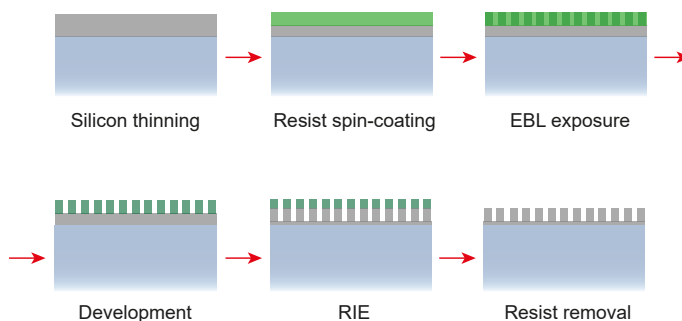


Figure 3.1: Fabrication steps needed for the metasurface sample.

Starting with the metasurface fabrication, we opted to fabricate the optimized geometry for 2nd-order differentiation as this symmetric structure is easier to obtain compared to the fully asymmetric one optimized for 1st-order differentiation.

The platform used for this sample is Silicon on sapphire (Al_2O_3). Indeed, high purity c-Si can be hetero-epitaxially grown on synthetic sapphire wafers and this CMOS technology is now well developed and commercially available. Using the experimental indices for the two materials [1, 2], the optimized dimensions for this design are $w = 206$ nm, $h = 142$ nm, and $p = 300$ nm with a thin residual Si layer (thickness $t = 20$ nm) that is intentionally left between the pillars. This layer is essential to achieve optimum transmission for large wavevectors, as discussed later.

In the following, the detailed fabrication procedure is explained step by step.

- c-Si on Al_2O_3 substrates were acquired from MTI corp. The c-Si (orientation: (100)) layer is 500 nm-thick, polished (surface roughness < 2.5 nm) and undoped. The sapphire (orientation: R -plane) substrate is 0.46 mm-thick and double-side polished (surface roughness < 0.3 nm on front side and optical grade polish on the back).
- The substrate was cleaned in base piranha and the c-Si was etched to the final metasurface thickness via Reactive Ion Etching (RIE) using Oxford Instrument's PlasmaPro 100 Cobra ICP and a three-step process employing Cl_2 , HBr and O_2 . The first steps is used to remove the native oxide on the Si layer:

Cl ₂ gas flow	50 [sccm]
pressure	7 [mTorr]
Set temperature	60 [°C]
RIE forward power	30 [W]
ICP power	750 [W]
time	11 [s]

Next, the system is pumped out for 2 minutes in order to completely remove any residual Cl₂. The third step etches the Si layer:

HBr gas flow	48 [sccm]
O ₂ gas flow	2 [sccm]
pressure	7 [mTorr]
Set temperature	60 [°C]
RIE forward power	30 [W]
ICP power	750 [W]
time	89 [s]

The recipe is run first on a dummy wafer to condition the chamber and then on the actual sample. The etch rate of the entire process is $h_{\text{etched}}(t) = 45 \pm 18 + (3.7 \pm 0.24)t$ where h_{etched} is the etched thickness in [nm] and t is the Si-step etch time in [s] (the Cl₂ etch step time is kept constant). The final c-Si thickness is checked with Filmetrics F20, an optical characterization tool that fits the Fabry-Pérot sample spectrum to obtain the thickness.

This fabrication step is quite tricky since the actual etch rate depends on the chamber conditions and on other poorly controllable parameters. Moreover, since the etch time is very long a small fluctuation on the etch rate can cause a relevant change in the final thickness.

- The substrate was cleaned again in base piranha and a 200 nm-thick layer of CSAR 62 (AR-P 6200, 9% in anisole) positive-tone resist (ALLRESIST GmbH) was spin-coated at 4000 rpm and baked for 2 minutes at 150°C.
- Lines were fabricated in the CSAR layer by exposure using a Raith Voyager lithography system (50 kV, dose 145–150 $\mu\text{C}/\text{cm}^2$) and development in Pentyl-acetate (60 s) and o-Xylene (10 s). One important detail concerning this step is that the nano-beams have to be aligned along the optical axis of sapphire during e-beam exposure. This is due to the fact that sapphire is a birefringent material and therefore has a refractive index that depends on the polarization impinging light. If the nanobeam arrays are aligned to the optical axis, light polarized along the wires length experiences only one refractive index.
- The pattern was then transferred into the c-Si by a three-step RIE process employing Cl₂, HBr and O₂. The latter, is almost identical to that described previously except for the ratio between the fluence of O₂ and HBr gases. This has an influence on the slanting of the final structure sidewall and an optimum slanting of

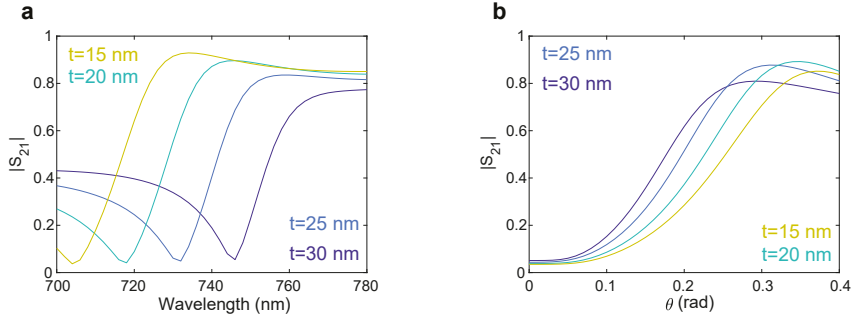


Figure 3.2: **a** Metasurface transmission spectrum for different residual thicknesses t . **b** Metasurface angular transmission S_{21} at the wavelength of the minimum for different values of t

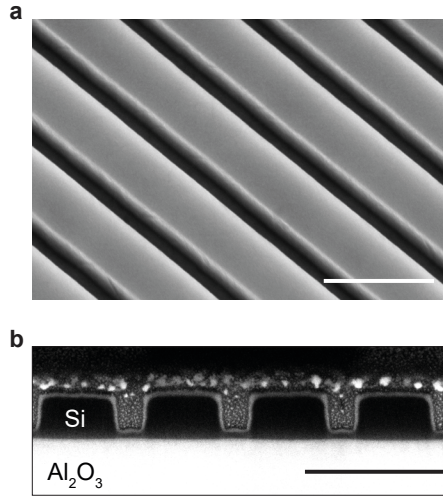


Figure 3.3: Experimental Si metasurface performing 2nd-order spatial differentiation. **a** Tilted SEM image of the Si metasurface performing the 2nd-derivative operation. **b** SEM image of a FIB cross section of the same metasurface showing the Si nanobeams on an Al_2O_3 substrate. The scale bar is 400 nm for both panels.

only 20 nm was achieved with 48.7 sccm for HBr and 1.4 sccm for O_2 .

Again, the etch time is an important parameter as it defines the residual thickness left in between the nanobeams. This, in turn, influences quite strongly the transmission spectra and the metasurface angular response, as shown in Figure 3.2.

- The sample was finally cleaned in anisole at 65°C followed by an acid piranha cleaning.

Figure 3.3 shows the result of the fabrication procedure. The sample are uniform over large areas (500 μm) with very low sidewall roughness. The FIB cross-section in Figure 3.3b highlights the low sidewall slanting and the thin (thickness $t \approx 22$ nm) Si residual layer.

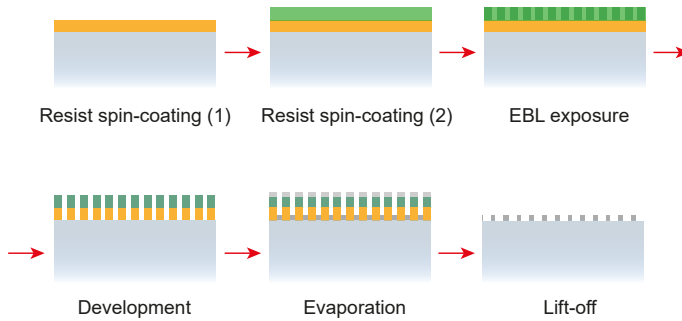


Figure 3.4: Fabrication steps needed for the images sample.

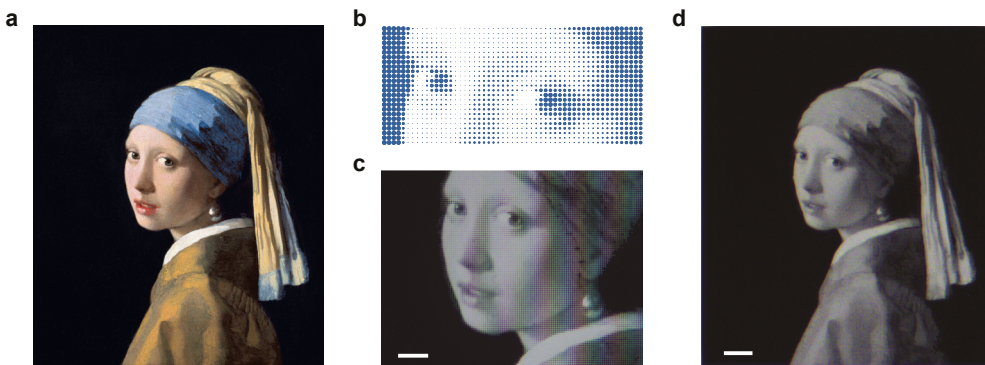


Figure 3.5: **a** *Meisje met de parel*, Johannes Vermeer circa 1665, oil on canvas, Mauritshuis, The Hague, Netherlands. **b** An array of suitably sized dots can imitate a gradient **c-d** Optical microscopy images of the final sample.

The fabrication procedure just described is an example of a top-down process in which a nanostructure is carved into a certain material. On the other hand, in order to fabricate the image samples a bottom-up process is used, as schematically shown in Figure 3.4. The following steps were performed to fabricate the samples:

- Glass slides (24×24 mm) were cleaned in base piranha.
- A bilayer of MMA (MMA(8.5)MAA EL9, 150 nm) and PMMA (PMMA 950k A8, 95 nm) was spin-coated and baked at 150°C and 180°C for 2 minutes respectively. The thickness of the layers has to be chosen carefully, very thick layers would lift-off easily in anisole but do not allow high resolution due to beam broadening during e-beam exposure and excessive MMA undercutting during development.
- The images were fabricated in the resist layer by exposure using Raith Voyager lithography system (50 kV, dose 550 $\mu\text{C}/\text{cm}^2$) and development in MIBK:IPA (1:3 for 90 s).

- A 40 nm thick Cr layer was evaporated using an in-house built thermal evaporator.
- The residual resist was lifted-off in anisole at 65°C facilitating the process with an ultra-sonicator.

Following this procedure, two-tone and gray-tone images were fabricated. To obtain the gradient effect in the gray-tone image, the famous painting *Meisje met de parel* (J. Vermeer, circa 1665) has been discretized into an array of suitably sized Cr disks. The final result looks homogeneous if low magnification ($< 60\times$) is used in a standard optical microscope (see Figure 3.5).

3.2. OPTICAL CHARACTERIZATION

The last experimental effort consists in characterizing optically the fabricated samples. First, the metasurface transfer functions has to be measured. Second, the image processing capabilities are tested by projecting the image sample onto the metasurface. These two different measurements are performed with two different setups that will be described in the following, along with the corresponding results.

3.2.1. INTEGRATING SPHERE

To experimentally determine the transfer function of the metasurface angle-resolved transmission ought to be measured. The data was collected with a Spectra Pro 2300i spectrometer equipped with a Pixis 400 CCD. The sample was mounted on a rotating stage and illuminated with collimated white light from a SuperK EXTREME/FIANIUM supercontinuum laser. The transmitted light was collected by an integrating sphere and sent to the spectrometer through a multimode fiber. Light was polarized along the nanobeams direction.

Figure 3.6a shows the measured transmittance ($T = |S_{21}|^2$) spectra as the incident angle is changed from 0 to 25°. In agreement with the simulated data in Figure 2.3, the Fano resonance shifts to shorter wavelengths as the angle is increased. The transmittance minimum is observed at $\lambda = 726$ nm for normal incidence and amounts to 2.2%, the residue attributed to minor fabrication imperfections. Figure 3.6b shows the transmittance as a function of the in-plane wavevector at $\lambda = 726$ nm, derived from the data in Figure 3.6a. The corresponding transmission amplitude ($|S_{21}|$) derived from the data is also plotted, along with the ideal parabolic amplitude response.

The overall trend with increasing transmittance as a function of angle is well reproduced experimentally, with a significant residual transmittance at normal incidence and a maximum amplitude at largest angle of 0.84, which is mostly determined by the absorption in Si. Employing alternative high-index materials could further enhance the transmission for large angles.

3.2.2. DUIMELIJN FOURIER MICROSCOPE

In order to assess the processing capabilities of the metasurfaces, an image is projected onto the sample and the outcome is inspected on a CCD camera using the optical setup

Duimelijntje is a fairy tale by the danish writer Hans Christian Andersen (published in 1836) and also the name given to the setup.

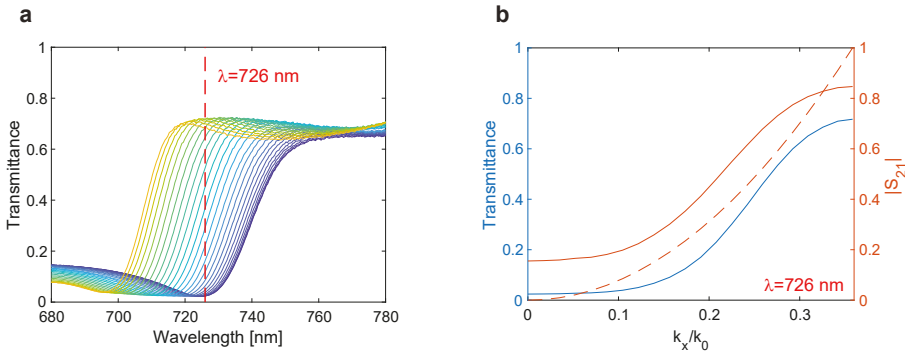


Figure 3.6: Experimental metasurface transmission. **a** Measured transmission spectra of the metasurface in Figure 3.3 as the angle of incidence is increased from 0 (blue line) to 25° (yellow line) in 25 steps. **b** Measured transmittance (blue line) and corresponding calculated (Transmittance = $|S_{21}|^2$) transmission amplitude $|S_{21}|$ (orange solid line) as function of incident in-plane wave vector k_x/k_0 at $\lambda = 726$ nm. The dashed orange line shows the ideal parabolic transfer function for $|S_{21}|$.

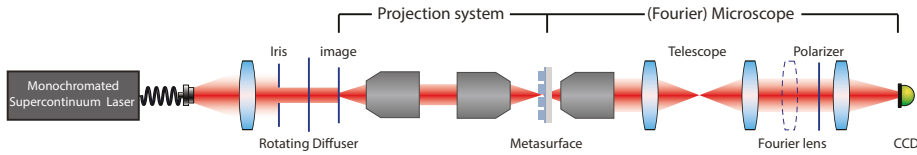


Figure 3.7: The setup consist of a projection system coupled to a standard microscope with Fourier imaging capabilities. The dashed line represent the removable Bertrand lens.

in Figure 3.7. The illumination is provided by a SuperK EXTREME/FIANIUM supercontinuum white light laser that is monochromated (1 nm bandwidth) by an Acousto-Optic Tunable Filter (AOTF) and subsequently coupled to a single mode fiber. The output of the fiber is collimated by a condenser lens and passed through a spinning diffuser plate to evenly illuminate the image which is composed of Cr patterns on glass. The diffuser also serves to remove speckle artefacts in imaging that otherwise occur due to the large spatial coherence of the source. The image is projected at unit magnification onto the metasurface by two Olympus MPlanFL N 20x-0.45NA objectives. The second half of the setup is a standard microscope with Fourier imaging capabilities, already reported in Ref.[3]: the image is collected by either of two objectives (Nikon Plan Fluor 20X – 0.5NA and Nikon S Plan Fluor ELWD 60X – 0.7NA) and projected onto a Photometrics CoolSNAP EZ silicon CCD camera by a 20 cm focal distance tube lens. In between objective and tube lens, a 1:1 telescope provides an intermediate real space plane, while flipping in the Fourier (or Bertrand) lens allows projection of the back focal plane of the objective directly onto the CCD[4] (Fourier imaging mode, unit magnification from back focal plane to objective).

This setup also allows transfer function amplitude measurements if the image and the first objective (from left) are removed and the Bertrand lens is flipped in. Indeed, using

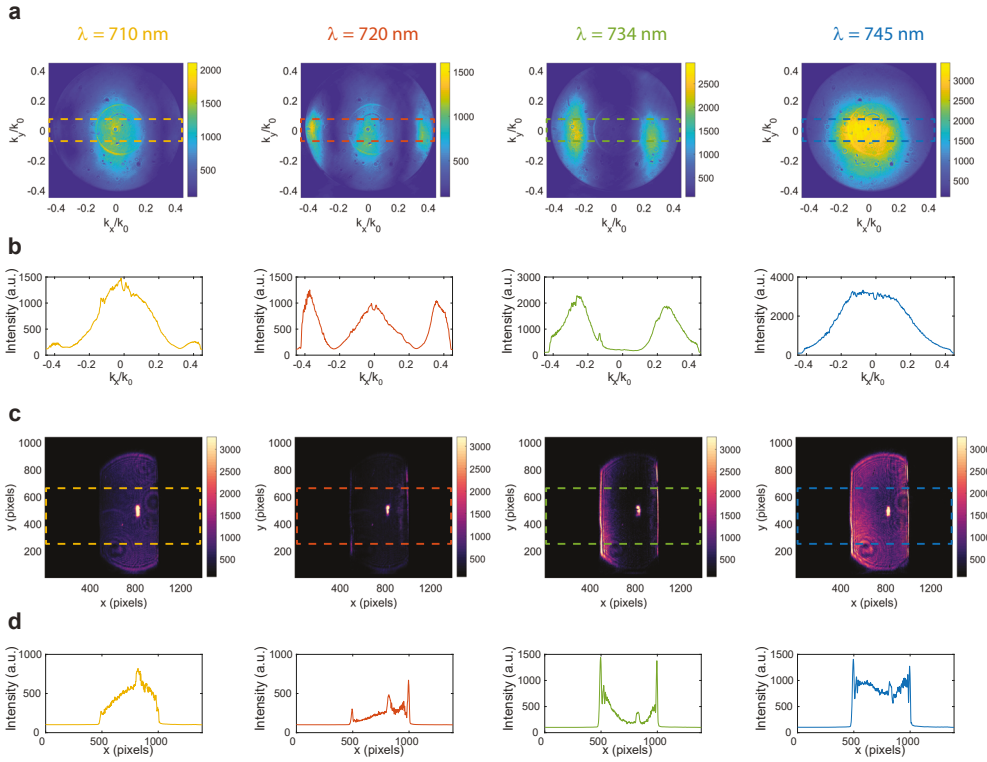


Figure 3.8: **a** Fourier space intensity map of light transmitted through the metasurface as the excitation wavelength is changed. **b** Average along the y -axis within the dashed box in **a**. **c** Image of the metasurface output as the excitation wavelength is changed. The input image is a slit. **d** Average along the y -axis within the dashed box in **c**.

this configuration, light transmitted through the metasurface under a certain span of angles (dependent on the objectives' NA) is imaged in k -space and therefore the amplitude of the metasurface transfer function can also be obtained. However, compared to the simpler transmission setup described above, normalization of the intensity is much more difficult and less reliable since it requires realignment and repositioning of the objectives. For this reasons, while this technique is very insightful and gives information also for $k_y \neq 0$, it is still preferable to use the integrating sphere and a rotating stage to measure quantitatively the transfer function.

Figure 3.8a shows such not normalized transfer function amplitudes as the excitation wavelength is scanned across the resonance. The dark blue regions in these colormaps signal the spatial components that the metasurface is rejecting, either by absorption or by reflection. As the wavelength is increased, the minima in k -space are moving closer to normal incidence ($\vec{k} = 0$): only on resonance it is possible to couple to the leaky mode from normal incidence, while for an off-resonant wavelength also an off-normal incident excitation is required, as expected from momentum matching. Furthermore, the

transfer function is completely transforming in a narrow bandwidth going from a low-pass spatial filter ($\lambda = 710$ nm) to an high-pass spatial filter on resonance. At $\lambda = 745$ nm the metasurface is not imparting any modulation in k -space and the Gaussian profile of light out-coupling from the fiber and scattered evenly from the diffuser is retrieved.

These measurements clearly show the 1D nature of the metasurface operation. In fact, on resonance low k_x spatial components are suppressed also for a wide range of k_y . Hence, the 2nd-order differentiation is experimentally performed in a line-by-line fashion, in agreement with the numerical calculation shown in Figure 2.9 of Chapter 2.

Flipping out the Bertrand lens and inserting the first objective and an image, it is possible to study the metasurface image processing corresponding to the transfer functions just discussed (see Figure 3.8c). In this case the image is a simple adjustable slit. At $\lambda = 710$ nm the metasurface is acting as a low-pass filter so the image of the slit is blurred and the edges are smoothed. On resonance the edges are clearly detected while off-resonance, for $\lambda = 745$ nm, the image of the slit is recovered. The bright spot in Figure 3.8c is an artefact due to spurious reflection at the interface between air and the sapphire substrate.

Finally, we experimentally investigate the 2nd-derivative operation of the Si metasurface when more complex images are projected onto the sample. We first project the image of one of our institutions' logos onto the metasurface using off-resonant illumination ($\lambda = 750$ nm) and then image the metasurface output onto the CCD (Figure 3.9b); the contrast of the input object is clearly maintained. On the other hand, for resonant illumination at $\lambda = 726$ nm (Figure 3.9c) the edges are clearly resolved in the transformed image. As expected, no edge contrast is observed for features along the x -direction since the derivative operation is performed along the same direction.

To study the edge profile in a quantitative manner, Figure 3.9d (red curve) shows a line profile taken along the horizontal direction in the processed image (red dashed line in Figure 3.9c). These data are compared to the calculated output profile assuming an ideal parabolic transfer function (blue curve in Figure 3.9d). Overall the experimental and ideal response show very similar trends: the double-peaked structure expected for 2nd-order differentiation is clearly resolved in all of the six edges shown in Figure 3.9d. The discrepancies between experimental and ideal response are probably due to minor misalignment of the sample inducing small asymmetries in the transfer function.

In conclusion, we demonstrate the use of a Si metasurface for the processing of a gray-tone image, like the *Meisje met de parel* described in the previous section. An off-resonant transmission image through the metasurface is shown in Figure 3.9f; the fine features and the contrast in the original object are clearly reproduced in the image. In contrast, the image processed at the resonant wavelength $\lambda = 726$ nm clearly shows the vertical edges along the face contour. The contours are fading away as they become gradually aligned with the x -axis, as expected. This clearly demonstrates that the metasurface image processing concept can be applied to more complex images containing gradients in transmission.

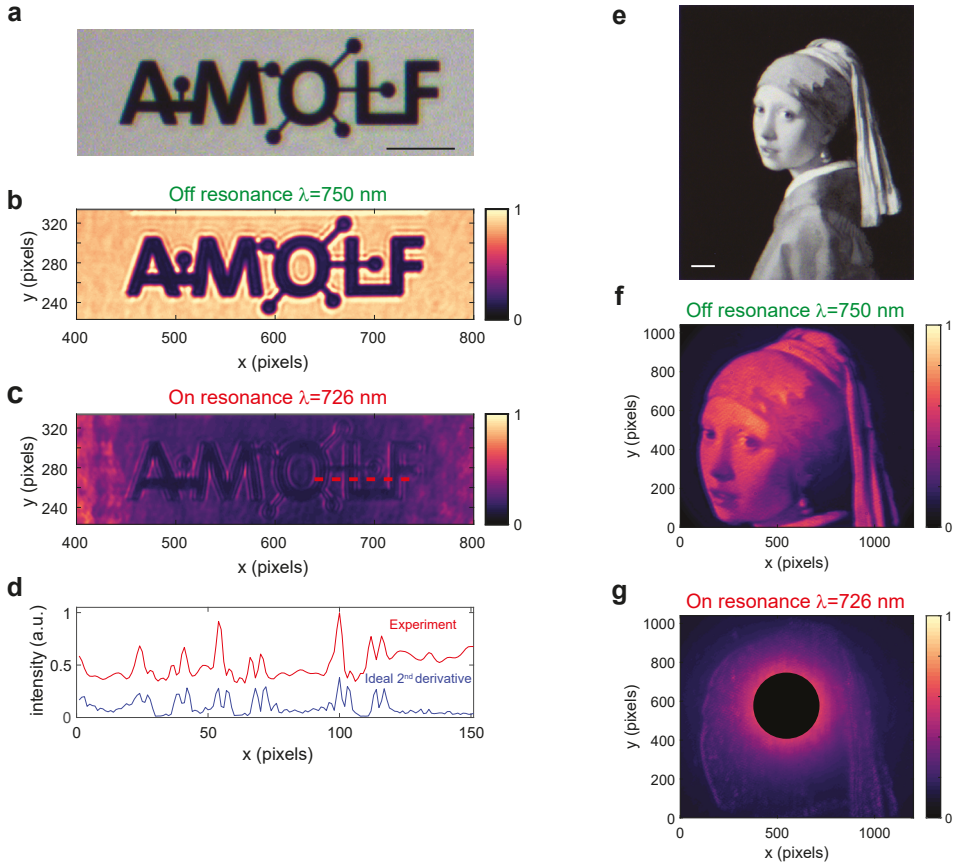


Figure 3.9: Experimental 2nd-order image differentiation. **a** Optical microscopy image of the input object; the scale bar is $20\mu\text{m}$. **b-c** Optical microscopy image of the metasurface output for resonant ($\lambda = 726\text{ nm}$) and off-resonant ($\lambda = 750\text{ nm}$) illumination. **d** Cross-cut through **b** (red line) averaged over 8 pixels along y , compared to ideal differentiation performed on the off-resonant image (blue line). **e** Optical microscopy image of the *Meisje met de parel* (J. Vermeer, circa 1665). The image is composed of micron-sized dots of Cr on glass. **f-g** Metasurface output for resonant and off-resonant excitation. The black spot in **g** covers an artefact due to spurious reflection at the interface between air and the sapphire substrate.

REFERENCES

- [1] I. H. Malitson and M. J. Dodge, *Refractive Index and Birefringence of Synthetic Sapphire*, in *Program of the 1972 Annual Meeting of the Optical Society of America*, Vol. 62 (1972) p. 1336.
- [2] M. A. Green, *Self-consistent optical parameters of intrinsic silicon at 300K including temperature coefficients*, *Solar Energy Materials and Solar Cells* **92**, 1305 (2008).
- [3] I. Sersic, C. Tuambilangana, and A. Femius Koenderink, *Fourier microscopy of single plasmonic scatterers*, *New Journal of Physics* **13**, 083019 (2011).
- [4] J. A. Kurvits, M. Jiang, and R. Zia, *Comparative analysis of imaging configurations and objectives for Fourier microscopy*, *Journal of the Optical Society of America A* **32**, 2082 (2015).

4

CONCLUSION

THE field of all-optical analog computing gained a lot of attention in the past and seemed for quite some time a promising alternative to standard electronic computing. However, as Moore's law kicked in, optical processors became quickly obsolete and were overwhelmed by what we nowadays mean by "computers".

The tremendous advances in nano-lithography the boosted the number of transistors per unit area played also a crucial role in the much younger field of Nanophotonics. Metamaterials, metasurfaces, photonic crystals, plasmonics and micro-resonators have demonstrated the possibility of molding the flow of light with unprecedented precision. From this perspective, optical analog computing is still an uncharted territory and the impact of Nanophotonics on this field can be groundbreaking.

In this context, the work presented in this thesis demonstrates how dielectric metasurfaces sustaining Fano resonances with suitably engineered dispersion can be designed to impart transfer functions in momentum space that correspond to 1st- and 2nd-order spatial differentiation. We showed that the ideal amplitude and phase transfer functions can be approximated over a relatively wide range of input angles spanning a numerical aperture up to 0.35 and that transmission over 0.8 can be achieved for large angles. The deviations from the ideal transfer functions, which are intrinsic to the design, are small enough to still achieve derivative operations close to 1st- and 2nd-derivative.

Furthermore, we experimentally demonstrated the metasurface optical processing using a suitably designed sub-wavelength array of Si nanobeams, showing clear edge detection as a result of the 2nd-order spatial differentiation and a significant agreement with the ideal response.

OUTLOOK

The results showed in this thesis can lead to a wide range of applications and can open new opportunities in hybrid optical and electronic computing that operates at low cost, low power and small dimensions. Future research directions could include:

- Demonstration of other mathematical operations including integration and con-

volution with specific functions. Also, the case of 1st-order spatial differentiation has still to be experimentally proved. This, in turn, would require upgrades to the setup described in Section 3.2.2 targeting phase measurements in order to assess the asymmetric phase response of odd operations.

- Design and performance improvement employing membranes and lossless dielectrics. The use of membranes could potentially remove the spurious bright spot due to reflection at the air-sapphire interface. Moreover, the use of lossless dielectric materials could boost the transmission at large k -vectors to unity, therefore enabling the ultimate processing efficiency.
- Theoretical and experimental demonstration of metasurfaces capable of performing 2D operations like $\nabla^2 = \frac{\partial^2}{\partial x^2} + \frac{\partial^2}{\partial y^2}$. In practical applications, this can be an interesting opportunity as all the edges would be detected regardless the orientation.
- Design and fabrication of optically and electrically switchable metasurfaces. The use of carrier-induced refractive index changes in ITO and optically-induced non-linearity in Si might lead to change in the transfer function that could switch the operation of choice. In addition, Si-based MEMS metasurface geometries that can be electrically actuated will also be taken into consideration.
- The implementation of analog recursive operations. By looping back the processed images onto the original image plane, subsequent mathematical operations can be achieved hinting at the dream of an optical computer.
- Metasurface dimensions and fabrication throughput scaling-up via Soft Conformal Imprint Lithography (SCIL). A silicon master pattern is made with electron-beam lithography and reactive ion etching, from which a soft double-layer PDMS stamp is molded. This stamp can be reused many times to pattern silica sol-gel masks for reactive ion etching. In this way, centimeter-sized metasurfaces can be readily replicated.

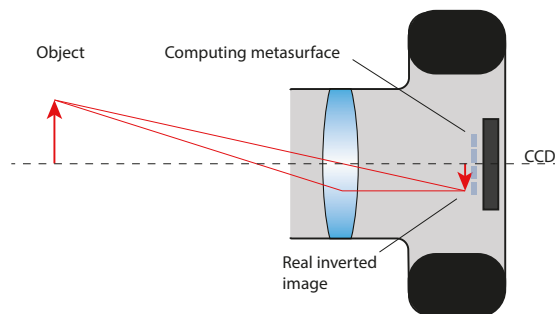


Figure 4.1: Ray diagram for a standard imaging system. The metasurface can be placed directly on the imaging sensor (CCD).

- Device integration. As our metasurface design operates in the image plane of the object and not in the Fourier plane it can be placed directly onto the CCD chip, as shown in Figure 4.1. This can lead to a wide range of applications and can readily be implemented in combination with standard CMOS technology.

To conclude, these and other opportunities will be explored in the near future at AMOLF (Amsterdam) in close collaboration with the group of Prof. Andrea Alù at ASRC (New York).

ACKNOWLEDGEMENTS

Dear Reader,

here's legitimately the most important part of this thesis, as none of this work would have been possible without the great support of many people who I would like to thank in the following.

Let me start with my splendid family whose unconditional support, encouragement and love have been always crucial during my journey.

I want to thank Albert for being such a great reference point in my scientific and non-scientific life. He's continuously providing me with great scientific opportunities and genuinely supporting my ideas and my academic growth. But, most importantly, I know that I can count on him no matter the nature of the issue that I'm facing (personal or work related). Having such a guide makes all the difference in a tough but exciting time such as the Ph.D.

Next, I would like to thank Andrea for the amazing time in Austin. His excitement about our work and the way he constantly challenged me has been an incredible drive and I look forward to working again with him.

This work would have never been possible without the precious collaboration with Femius. Working with him has been fun and I really appreciate his willingness to share his deep knowledge about Photonics and also his jokes (including his funny looks!).

This thesis is also the end of a long and intense experience at the Scuola Superiore di Catania for which I'd like to thank my tutor prof. Francesco Priolo and prof. Giuseppe Angilella who took good care of me since we met almost 8 years ago.

My time in Austin has been very exciting thanks to the awesome people in Andrea's group. I want to thank Hoyeong and Dimitrios for their crucial help in setting up the theory for this work but also for the trip to the White Sands, Austin City Limits, the GP of The Americas and the countless cheerful moments together. Let me also mention the Caffè Lorentz founders Yarden, Michele, Sander, and Giuseppe who made every lunch break so enjoyable. I would also like to thanks the Grad students of the group who made me feel part of it from the first day: Misha, Ahmed (K), Ahmed (M), Matt, Curtis, Diego, Guangwei, Li, Siyuan, Yoshi, Zhicheng and Bobby (thanks for organizing my first Thanksgiving!).

Special thanks go to the Photonic Materials group! The start of my Ph.D. could not have been more exciting and this is due to the fantastic people I'm working with every day. Thanks for the beers on Fridays, the random outings at the Waterkant and Biertuin and most importantly for making my time here truly *gezellig*!

Let me also thank all the people at AMOLF who make it such a magical place: the clean-room guys (Bob, Dmitry, Andries and Hans), the Duimelijn folks (Marko, Christiaan, Hugo and Ruslan), Alessandro, Marco, Giorgio, Robin, Julia, Carolyn, Agustin, Lukas, Christian, chutya (Harshal), Jenny, John, Kevin, Lucie, Moritz, Nikhil, Annemarie, Biplab,

Giada, Lorenzo, Nasim, Sven, Benjamin, Said, Dion, Piero, and Vanessa.

Furthermore, big thanks to Loret(t)a for the countless coffee breaks, pizzas at Bella Storia, for sharing his passion about trashy tv and for being such a lovely traveling companion during this adventure.

Dulcis in fundo, thanks to Claudia who literally followed me around the world during the last two years showing me what means to care about someone special.

A

APPENDIX

This appendix contains the omitted calculations of Chapter 2. Specifically, the scattering matrix formalism and the Coupled-mode-theory model used are shown in a step by step fashion.

A.1. SCATTERING MATRIX FORMALISM

Light interaction with a generic optical system may be described by a set of linear equations which relate incident, transmitted and reflected wave amplitudes. These linear relationships define a matrix called *scattering matrix* or *S – matrix*. In particular, it relates the outgoing complex wave amplitudes \mathbf{s}_- to the incoming complex wave amplitudes \mathbf{s}_+ . For a two ports configuration¹

$$\begin{pmatrix} s_{1-} \\ s_{2-} \end{pmatrix} = \begin{pmatrix} S_{11} & S_{12} \\ S_{21} & S_{22} \end{pmatrix} \begin{pmatrix} s_{1+} \\ s_{2+} \end{pmatrix} \quad \leftrightarrow \quad \mathbf{s}_- = \mathbf{S}\mathbf{s}_+ \quad (\text{A.1})$$

where the complex wave amplitudes are defined and normalized such that, for example, $|s_{1+}|^2$ is the power per unit area incident on the the system

$$s_{1+} = \sqrt{\frac{cn_0\epsilon_0}{2}} \mathbf{E}_{1+} \quad (\text{A.2})$$

with analogous definitions for the remainder components of the vectors \mathbf{s}_- and \mathbf{s}_+ . General requirements such as energy conservation, reciprocity and time reversibility constrain the matrix elements of \mathbf{S} [3].

First, if the system is lossless all the energy pumped into the system has to go out. Hence power conservation implies

$$|s_{1+}|^2 + |s_{2+}|^2 = |s_{1-}|^2 + |s_{2-}|^2 \quad \leftrightarrow \quad \mathbf{s}_+^\dagger \mathbf{s}_+ = \mathbf{s}_-^\dagger \mathbf{s}_- \quad (\text{A.3})$$

Parts of this chapter have been re-adapted from Refs.[1, 2].

¹It is straightforward to generalize this to a m port system using a $M \times M$ scattering matrix

and using $\mathbf{s}_- = S\mathbf{s}_+$

$$\mathbf{s}_+^\dagger \mathbf{s}_+ = \mathbf{s}_+^\dagger S^\dagger S \mathbf{s}_+ \rightarrow \mathbf{s}_+^\dagger \mathbf{s}_+ - \mathbf{s}_+^\dagger S^\dagger S \mathbf{s}_+ = 0 \quad (\text{A.4})$$

$$\rightarrow \mathbf{s}_+^\dagger [\mathbb{I} - S^\dagger S] \mathbf{s}_+ = 0 \quad \forall \mathbf{s}_+ \Rightarrow S^\dagger S = \mathbb{I} \quad (\text{A.5})$$

where \mathbb{I} is the identity matrix. The constraint implied by unitarity on the matrix elements are

$$\begin{cases} |S_{11}|^2 + |S_{12}|^2 = 1 \\ |S_{22}|^2 + |S_{21}|^2 = 1 \\ S_{11}^* S_{12} + S_{21}^* S_{22} = 0 \end{cases}$$

Another property that holds for lossless media is *time reversibility*. To show its implications on the S – matrix elements the complex conjugate of (A.1) is taken

$$\mathbf{s}_-^* = S^* \mathbf{s}_+^* \quad (\text{A.6})$$

The complex wave amplitudes \mathbf{s}_-^* may be interpreted as time reversed out-going wave amplitudes thus incoming wave amplitudes ($\mathbf{s}_-^* \rightarrow \mathbf{s}_+$) and the same reasoning applies for \mathbf{s}_+^* (i.e. $\mathbf{s}_+^* \rightarrow \mathbf{s}_-$). With these substitutions (A.1) becomes

$$\mathbf{s}_+ = S^* \mathbf{s}_- \rightarrow \mathbf{s}_- = [S^*]^{-1} \mathbf{s}_+ \quad (\text{A.7})$$

Comparing this last equation with (A.1) yields

$$[S^*]^{-1} = S \quad \text{or} \quad S^* = S^{-1} \quad (\text{A.8})$$

This condition together with the first discussed property $S^\dagger = S^{-1}$ leads to

$$S^\top = S \quad (\text{A.9})$$

This same result can be obtained also from the reciprocity principle for an isotropic medium. Therefore time reversibility and power conservation imply reciprocity [3].

A.2. COUPLED MODE THEORY

The *Coupled Mode Theory* (CMT) formalism is very powerful in describing the behavior of a resonator coupled to input and output ports. This theory has been developed mainly by Hermann Haus [3] and further refined by Shanhui Fan et al.[4]. Moreover, it enables the possibility of calculating the transmission of an optical system by modeling its interaction with incoming light through a direct process and a resonant process. Thus, it is a valuable tool to model guided–mode–resonances.

The first step consists in defining the optical system and the output and input planes. Hence, suppose our resonant structures (nanopillars or nanowires) are enclosed inside a "black box" simply stating that the complex field inside the box is u (normalized such that $|u|^2$ is the energy stored within the box due to the resonance) and that this system has a certain resonance frequency ω_0 . In our case the latter is a guided–mode–resonance, however within the frame of CMT there is no need to further specify the nature of the resonance.

The outgoing wave amplitudes \mathbf{s}_- are the result both of the box's leakage and of the action of a scattering matrix \mathbf{C} , which would describe the system if the resonances were turned off, to the incoming wave amplitudes \mathbf{s}_+

$$\mathbf{s}_- = \mathbf{C} \mathbf{s}_+ + u \mathbf{d} \quad (\text{A.10})$$

where $\mathbf{d} = (d_1, d_2)^\top$ is a vector of coupling coefficients. As mentioned in Chapter 2, the direct process is modeled by the interaction of light with a dielectric slab of index $n_{\text{eff}} = [(1 - F)n_0^2 + Fn^2]^{1/2}$ (with $n = 4$) in air ($n_0 = 1$) where F is the structure fill-factor[5]. Thus in our model (A.10) reads

$$\begin{pmatrix} s_{1-} \\ s_{2-} \end{pmatrix} = \begin{pmatrix} r & t \\ t & r \end{pmatrix} \begin{pmatrix} s_{1+} \\ 0 \end{pmatrix} + u \begin{pmatrix} d_1 \\ d_2 \end{pmatrix} \quad (\text{A.11})$$

where r and t are the Fresnel coefficients for a Fabry-Pérot etalon of thickness d equal to the height of the metasurface

$$r = \frac{r_1 + r_2 e^{-2i\delta}}{1 + r_1 r_2 e^{-2i\delta}} \quad t = \frac{t_1 t_2 e^{-i\delta}}{1 + r_1 r_2 e^{-2i\delta}} \quad (\text{A.12})$$

r_1, r_2, t_1, t_2 , are the standard Fresnel reflection and transmission coefficients for the two slab interfaces and $\delta = (2\pi/\lambda) n_{\text{eff}} d \cos\theta_1$ (θ_1 is the angle at which light is refracted inside the slab in case of not normal incidence).

Equation (A.11) shows clearly that the output of the optical system is the sum of a direct process (first product in the right-hand side) and a resonant process (second product in the right-hand side). Notice that s_{2+} is zero since no light is coming from the substrate.

Coupled to (A.11), another equation is needed to describe the complex field inside the system

$$\frac{du}{dt} = (i\omega_0 - \gamma) u + \kappa_1 s_{1+} \quad (\text{A.13})$$

being γ the radiative leakage and κ_1 the coupling coefficient for s_{1+} pumping the resonator². In the frequency domain $\frac{d}{dt} \rightarrow i\omega$ therefore, from (A.13)

$$i\omega u = (i\omega_0 - \gamma) u + \kappa_1 s_{1+} \quad \rightarrow \quad u = \frac{\kappa_1 s_{1+}}{i(\omega - \omega_0) + \gamma} \quad (\text{A.14})$$

The product of (A.11) leads instead to

$$\begin{cases} s_{1-} = r s_{1+} + u d_1 \\ s_{2-} = t s_{1+} + u d_2 \end{cases}$$

Using the second equation of this system and (A.14) it is straightforward to write the following expression for s_{2-}

$$s_{2-} = t s_{1+} + \frac{d_2 \kappa_1 s_{1+}}{i(\omega - \omega_0) + \gamma} \quad (\text{A.15})$$

² κ_1 is the first component of the vector κ of coupling coefficients

and to define the quantity

$$S_{21} = \frac{s_{2-}}{s_{1+}} = t + \frac{d_2 \kappa_1}{i(\omega - \omega_0) + \gamma} \quad (\text{A.16})$$

This last quantity is of great importance in our derivation since the transmittance of the whole system is $T = |S_{21}|^2$ as can be noted recalling the definitions of \mathbf{s}_- and \mathbf{s}_+ . However, (A.16) is not our final result. Indeed, the coupling coefficients showing in the last equation cannot be unbound since the reflection itself is bound to be $T \leq 1$. Actually they are constrained by the direct pathway through these properties [4, 6, 7]

$$\mathbf{d}^\dagger \mathbf{d} = 2\gamma \quad (\text{A.17})$$

$$\kappa = \mathbf{d} \quad (\text{A.18})$$

$$\mathbf{C} \mathbf{d}^* = -\mathbf{d} \quad (\text{A.19})$$

where \mathbf{C} is a generic scattering matrix describing the direct pathway and γ is the sum of the leakage rates into the ports.

These properties³ and those previously discussed regarding the S -matrix will be of great use in further refining the expression obtained for S_{21} . Indeed, applying (A.18) to (A.16) and exploiting the mirror symmetry of the problem ($d_1 = \pm d_2$, the sign being chosen according to the even or odd symmetry of the resonant mode)[4]

$$S_{21} = t \pm \frac{d_1^2}{i(\omega - \omega_0) + \gamma} \quad (\text{A.20})$$

Furthermore, (A.17) and (A.19) will enable the possibility of deducing an expression for d_1^2 . In our case $\mathbf{C} \mathbf{d}^* = -\mathbf{d}$ reads

$$\begin{pmatrix} r & t \\ t & r \end{pmatrix} \begin{pmatrix} d_1^* \\ \pm d_1^* \end{pmatrix} = - \begin{pmatrix} d_1 \\ \pm d_1 \end{pmatrix} \quad (\text{A.21})$$

and performing the product the following expression for d_1 is extracted

$$d_1^* (r \pm t) = -d_1 \quad (\text{A.22})$$

next, multiplying the latter for d_1 and using (A.17)

$$d_1^2 = -(r \pm t)\gamma \quad (\text{A.23})$$

Hence, the final expression used in Chapter 2 for the transmission S_{21} is

$$S_{21} = t \pm \frac{-(r \pm t)\gamma}{i(\omega - \omega_0) + \gamma}$$

Before moving on, it is worth commenting this last result. This relatively simple equation elegantly embodies the intuitive working principle of our structure and highlights

³The detailed proofs will be discussed in the next section

the origin of the Fano asymmetric lineshape. The quantity S_{21} is evidently the sum of two terms: t is simply the Fresnel coefficient for a dielectric slab and plays the role of the *direct pathway* mentioned earlier while the second term is due to the resonant behavior displayed by our structure and hence is referred to as *resonant pathway*. Furthermore, the direct path itself contains the resonant path (A.23) as a consequence of the constraints imposed ultimately by fundamental concepts such as energy conservation and time-reversal symmetry.

Since the two terms appearing in S_{21} are complex numbers, it is important to study their relative phase difference to understand how that influences the shape parameter, as discussed in Chapter 2.

A.2.1. PROOFS OF PROPERTIES (A.17) - (A.19)

For ease of notation the properties above will be proved for a single port resonator and then generalized. Hence (A.11) and (A.13) become

$$\frac{du}{dt} = (i\omega_0 - \gamma)u + \kappa s_{1+} \quad (\text{A.24})$$

$$s_{1-} = Cs_{1+} + du \quad (\text{A.25})$$

where C is now a number and γ is the leakage into the only port.

Proof. $dd^* = 2\gamma$

Suppose that the incoming wave amplitudes are turned off ($s_{1+} = 0$). Using (A.24)

$$\begin{aligned} \frac{d|u|^2}{dt} &= \frac{duu^*}{dt} = u \frac{du^*}{dt} + u^* \frac{du}{dt} = \\ &= u [(-i\omega_0 - \gamma)u^*] + u^* [(i\omega_0 - \gamma)u] = \\ &= -i\omega_0 |u|^2 - \gamma |u|^2 + i\omega_0 |u|^2 - \gamma |u|^2 = -2\gamma |u|^2 \\ \Rightarrow \frac{d|u|^2}{dt} &= -2\gamma |u|^2 \end{aligned}$$

Since $|u|^2$ is the energy stored inside the resonator and given the definition of s_{1-} , power conservation implies

$$\begin{aligned} \frac{d|u|^2}{dt} &= -|s_{1-}|^2 = -|d|^2 |u|^2 = -dd^* |u|^2 \\ \Rightarrow \frac{d|u|^2}{dt} &= -dd^* |u|^2 \end{aligned}$$

Looking at both the results it is clear that $dd^* = 2\gamma$. □

Proof. $\kappa = d$

Again, if the incoming wave amplitudes are turned off ($s_{1+} = 0$) it is straightforward to give a solution for (A.24)

$$\left\{ \begin{array}{l} \frac{du}{dt} = (i\omega_0 - \gamma)u \\ s_{1-} = du \end{array} \right. \rightarrow \left\{ \begin{array}{l} u = Ae^{(i\omega_0 - \gamma)t} \\ s_{1-} = dAe^{(i\omega_0 - \gamma)t} \end{array} \right.$$

where A is a constant. As expected, the energy stored inside the resonator decays with time as does the amplitude of the outgoing wave s_{1-} . Next, a time-reversal transformation is performed

$$\begin{cases} u(t) \rightarrow u^*(-t) \\ s_{1-}(t) \rightarrow s_{1-}^*(-t) \end{cases} \rightarrow \begin{cases} u^* = A^* e^{(i\omega_0 + \gamma)t} \\ s_{1-}^* = d^* A^* e^{(i\omega_0 + \gamma)t} \end{cases}$$

In this new configuration an exponentially growing incoming wave amplitude is building-up the energy stored from 0 at $t = -\infty$ to $|A|^2$ at $t = 0$.

The coupled equations describing this new situation are

$$\frac{du^*}{dt} = (i\omega_0 - \gamma)u^* + \kappa s_{1-}^* \quad (\text{A.26})$$

$$0 = C s_{1-}^* + d u^* \quad (\text{A.27})$$

in a similar manner as done previously to obtain (A.14), from these last two equation

$$u^* = \frac{\kappa s_{1-}^*}{i(\omega - \omega_0) + \gamma} \quad (\text{A.28})$$

The complex field u^* is driven by s_{1-}^* at a frequency ω_0 and with an amplitude growing at the rate γ . Thus the complex frequency of the drive is $\tilde{\omega} = \omega_0 + i\gamma$ and also the complex field u^* will have the same

$$\begin{aligned} u^*(\tilde{\omega}) &= \frac{\kappa s_{1-}^*}{i(\omega_0 - i\gamma - \omega_0) + \gamma} = \frac{\kappa s_{1-}^*}{2\gamma} = \frac{\kappa d^* u^*}{2\gamma} \\ \rightarrow u^* &= \frac{\kappa d^* u^*}{2\gamma} \Rightarrow 1 = \frac{\kappa d^*}{2\gamma} \end{aligned}$$

where $s_{1-}^* = d^* u^*$ has been used⁴. From this last result it follows that $\kappa d^* = 2\gamma$ and exploiting the property proved earlier $dd^* = 2\gamma$ it is evident that $\kappa = d$ \square

Proof. $Cd^* = -d$

Starting from the time-reversed situation discussed above, notice that no outgoing wave shall occur i.e.

$$0 = C s_{1-}^* + d u^*$$

exploiting again $s_{1-}^* = d^* u^*$ the property is proved

$$0 = C d^* u^* + d u^* \quad \forall u \Rightarrow C d^* = -d$$

\square

The three properties just shown can be generalized for a multi-port resonator obtaining (A.17), (A.18) and (A.19). In particular (A.17) for m ports is equivalent to

$$d_1^* d_1 + d_2^* d_2 + \dots d_m^* d_m = \sum_i \gamma_i = \gamma$$

⁴Notice that this substitution is valid only at $t=0$. In fact, s_{1-}^* is a function growing from 0 at $t = -\infty$ to $d^* A^*$ at $t = 0$ while s_{1-} is decreasing from dA at $t = 0$ to 0 at $t = +\infty$. Thus s_{1-}^* is the complex conjugate of s_{1-} only at $t=0$

being γ_i the leakage into port i . Further, from the equation above it can be set

$$\begin{aligned}d_1^* d_1 &= \gamma_1 \\d_2^* d_2 &= \gamma_2 \\&\dots \\d_m^* d_m &= \gamma_m\end{aligned}$$

REFERENCES

- [1] A. Cordaro, *All-silicon metasurfaces for anti-reflection*, Masters' thesis, Stanford University, University of Catania (2017).
- [2] A. Cordaro, J. van de Groep, S. Raza, E. F. Pecora, F. Priolo, and M. L. Brongersma, *Antireflection High-Index Metasurfaces Combining Mie and Fabry-Pérot Resonances*, *ACS Photonics* **6**, 453 (2019).
- [3] H. A. Haus, *Waves and fields in optoelectronics* (Prentice-Hall, Englewood Cliffs, N.J, 1984) p. 402.
- [4] S. Fan, W. Suh, and J. D. Joannopoulos, *Temporal coupled-mode theory for the fano resonance in optical resonators*, *Journal of the Optical Society of America. A* **20**, 569 (2003).
- [5] D. L. Brundrett, E. N. Glytsis, and T. K. Gaylord, *Homogeneous layer models for high-spatial-frequency dielectric surface-relief gratings: conical diffraction and antireflection designs*, *Applied Optics* **33**, 2695 (1994).
- [6] K. X. Wang, Z. Yu, S. Sandhu, and S. Fan, *Fundamental bounds on decay rates in asymmetric single-mode optical resonators*, *Optics Letters* **38**, 100 (2013).
- [7] K. X. Wang, Z. Yu, S. Sandhu, V. Liu, and S. Fan, *Condition for perfect antireflection by optical resonance at material interface*, *Optica* **1**, 41 (2014).

CURRICULUM VITÆ

Andrea CORDARO

26-04-1992 Born in Catania, Italy.

EDUCATION

2014	Bachelor's degree - Physics Università degli Studi di Catania <i>Thesis:</i> Trattazione quantistica di guide d'onda plasmoniche: nanowires d'oro <i>Promotor:</i> Prof. dr. G. Piccitto
2011–2016	Diploma - Classe delle scienze sperimentali Scuola Superiore di Catania <i>Tutor:</i> Prof. dr. F. Priolo
2017	Master's Degree - Condensed Matter Physics Università degli Studi di Catania <i>Thesis:</i> All-silicon metasurfaces for anti-reflection <i>Promotor:</i> Prof. dr. M.L. Brongersma Prof. dr. F. Priolo
2017 - present	Ph.D. - Physics AMOLF <i>Promotor:</i> Prof. dr. A. Polman Prof. dr. A. Alù
2016	Visiting Student Researcher Stanford University
2017-2018	Visiting Student The University of Texas at Austin

AWARDS

2015	“Premio G. Raciti” prize for Bachelor's thesis and career - Physics Department
2011	Scholarship “Premio incentivante” - Physics Department
2010-2011	Gold Medal - regional phase of Italian Physical Olympiads

LIST OF PUBLICATIONS

7. **A. Cordaro**, H. Kwon, D. Sounas, A. Femius Koenderink, A. Alù and A. Polman, *High-index dielectric metasurfaces performing mathematical operations*, (submitted).
6. **A. Cordaro**, J. van de Groep, S. Raza, E. F. Pecora, F. Priolo and M. L. Brongersma, *Antireflection High-Index Metasurfaces Combining Mie and Fabry-Pèrot Resonances*, [ACS Photonics](#) **6**, 453 (2019).
5. H. Kwon, D. Sounas, **A. Cordaro**, A. Polman and A. Alù, *Nonlocal Metasurfaces for Optical Signal Processing*, [Physical Review Letters](#) **121**, 173004 (2018).
4. E. F. Pecora, **A. Cordaro**, P. G. Kik and M. L. Brongersma, *Broadband Antireflection Coatings Employing Multiresonant Dielectric Metasurfaces*, [ACS Photonics](#) **5**, 4456 (2018).
3. **C.E.A. Cordaro**, E. F. Pecora, M. L. Brongersma, J. Van de Groep *Broadband, polarization-independent, omnidirectional, metamaterial-based antireflection coating*, [Worldwide patent applications](#), US Patent WO2018175874A1.
2. **A. Cordaro**, H. Kwon, D. Sounas, A. Polman and A. Alù, *Non-local computing metasurfaces performing mathematical operations*, [2018 Conference on Lasers and Electro-Optics \(CLEO\)](#), San Jose, CA, 2018, pp. 1-2.
1. **C.E.A. Cordaro**, G. Piccitto and F. Priolo, *Quantum plasmonic waveguides: Au nanowires*, [Eur. Phys. J. Plus](#) **132**, 453 (2017).

